Palaeogeography, Palaeoclimatology, Palaeoecology 645 (2024) 112217

Contents lists available at ScienceDirect

Palaeogeography, Palaeoclimatology, Palaeoecology

journal homepage: www.elsevier.com/locate/palaeo

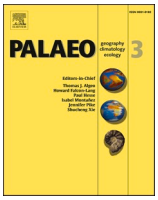

Structure of the eastern Arabian Sea upper water column in the middle Miocene: Implications for the development of the South Asian monsoon

Shixian Zou [a,1], Guanyu Lin [a,1,2], Anran Chen [a], Yueli Huang [a], Jeroen Groeneveld [b], Stephan Steinke [a,*], Liviu Giosan [c,d]

[a] Department of Geological Oceanography and State Key Laboratory of Marine Environmental Science, College of Ocean and Earth Sciences, Xiamen University, Xiamen, China
[b] Institute of Oceanography, National Taiwan University, Taipei, Taiwan
[c] Geology and Geophysics, Woods Hole Oceanographic Institution, Woods Hole, USA
[d] Research Institute of the University of Bucharest (ICUB), Bucharest University, Bucharest, Romania

ARTICLE INFO

Editor: Dr. Howard Falcon-Lang

Keywords:
Planktic foraminifera
Stable oxygen isotopes
Mg/Ca palaeothermometry
Upper ocean thermal gradient
Mixed layer depth
Thermocline depth

ABSTRACT

Global atmospheric circulation experienced drastic changes during the Middle Miocene climate transition (MMCT~14.7–13.0 Ma) possibly related to the glaciation on West-Antarctica. Palaeoceanographic reconstructions have found that upwelling in the western Arabian Sea due to summer South Asian monsoon (SAM) winds likely occurred since ~14.7 Ma, with fully modern-like monsoonal wind patterns after the end of the MMCT at around ~13 Ma. Whether the changes in monsoonal circulation since ~14.7 Ma are also associated with upper ocean hydrographic changes in the eastern Arabian Sea (EAS) is currently not known for the middle Miocene. To this end, the difference in Mg/Ca-based temperatures (ΔT°C) of surface-dwelling with lower mixed layer/thermocline-dwelling and sub-thermocline-dwelling planktic foraminifera was reconstructed to estimate the upper ocean thermal gradient at Site NGHP-01-01 A in the EAS and thus changes in the upper surface water column structure, i.e., mixed layer depth (MLD) and the depth of thermocline (DOT). The Mg/Ca-temperature estimates from the upper mixed layer down to the sub-thermocline show a prominent cooling trend between ~14.2 Ma and 13.2 Ma. The upper water column reconstructions reveal weaker mixing, a shallower thermocline, and therefore a well stratified upper water column in the EAS after ~14.2 Ma. We suggest that the weaker mixing and shallower thermocline in the EAS after ~14.2 Ma are most likely due to an intensification of the summer SAM. A strong salinity stratification and/or the formation of a barrier layer (BL) because of increased SAM rainfall and advection of low salinity water may also have contributed to a weaker mixing and shallower thermocline in the EAS during the investigated time period. The change in the upper ocean hydrography in the EAS after ~14.2 Ma fits well into the emerging picture of monsoonal-driven upper ocean hydrographic changes in the equatorial and northern Indian Ocean due to an intensification of the summer SAM since ~14.7 Ma.

1. Introduction

The South Asian Monsoon (SAM), as an important component of the global monsoon system, is one of the most intense climatic phenomena on Earth characterized by seasonal reversals in wind direction and changes in rainfall and is an important conveyor of interhemispheric exchange of moisture and energy (e.g., Webster et al., 1998; Viswambharan and Mohanakumar, 2014). Recent numerical model simulations suggest that the establishment of a modern-like South Asian monsoon summer circulation was associated with the uplift of Eastern African and Anatolian-Iranian landforms, which intensified and redirected the Somali Jet, which is the dominant low-level wind pattern over the Arabian Sea towards the Indian subcontinent, allowing the advection of moisture towards Asia during summer (Zhang et al., 2014; Sarr et al., 2022; Tardif et al., 2023). Those model simulations also show that strong upwelling in the western Arabian Sea (WAS) was only established after the full emergence of the Arabian Peninsula (Zhang et al., 2014; Sarr et al., 2022). Palaeorecords of upwelling and thus monsoonal wind strength in

* Corresponding author.
E-mail address: ssteinke@xmu.edu.cn (S. Steinke).
[1] Contributed equally to this study.
[2] Now at: CNOOC International Ltd., Exploration Technology Research Institute, Beijing, China

https://doi.org/10.1016/j.palaeo.2024.112217
Received 17 August 2023; Received in revised form 17 April 2024; Accepted 18 April 2024
Available online 19 April 2024

the WAS place the onset of modern summer South Asian Monsoon (SAM) wind patterns at ~12.9 Ma (Gupta et al., 2015; Betzler et al., 2016). However, evidence for an earlier intensification of modern SAM wind patterns comes from sea surface temperature (SST) records (Zhuang et al., 2017) and sedimentary geochemical tracers (Bialik et al., 2020) in the WAS, which suggest that the upwelling in the WAS and oxygen minimum zone (OMZ) in the Arabian Sea were most likely initiated between ~14.7 and 14.0 Ma, possibly closely related to the glaciation of western Antarctica during that time. The first appearance of planktic foraminifera *Globigerina bulloides*, an indicator of upwelling conditions, in the WAS at ~14.5 Ma (Kroon et al., 1991) is also in agreement with an earlier intensification of upwelling and thus monsoonal winds in the WAS. A recent study found that summer SAM winds likely drive upwelling in the WAS since ~14.7 Ma after the Miocene Climatic Optimum (MCO; ~16.9–14.7 Ma), with fully modern-like monsoonal wind patterns since the end of the Middle Miocene Climatic Transition (MMCT) ~13 Ma (Auer et al., 2023).

Whether the strengthening of monsoonal atmospheric circulation as inferred from proxy records from the WAS since ~14.7 Ma is also associated with upper ocean hydrographic changes in the eastern Arabian Sea (EAS), i.e., changes in mixed layer (MLD) and depth of the thermocline (DOT) is currently not known for the middle Miocene. Monsoon wind-induced changes in the upper water column structure of the EAS have been reconstructed so far only for the Oligocene-early Miocene (30–20 Ma; Beasley et al., 2021) and the early Pleistocene (Satpathy et al., 2019). Beasley et al. (2021) have found an increase in water column ventilation and water mass mixing, indicating an increase in winter monsoon type atmospheric circulation, possibly driven by a relative southward shift of the intertropical convergence zone between 23.7 and 23.0 Ma and an intensification of a proto-summer SAM system at around ~23.0 Ma to 22.7 Ma. Satpathy et al. (2019) have reported a more stratified upper water column during the period ~2.7–1.85 Ma, which is interpreted to reflect an overall weaker winter SAM circulation and enhanced mixing between ~1.55 Ma and 1.65 Ma, which was probably driven by an intensification of the winter SAM winds. A study from the eastern equatorial Indian Ocean noted a shallow thermocline during the latest Miocene - Early Pliocene (between ~6 and 3.4 Ma), reflecting an intense summer SAM and a deepening of the thermocline and thickening of the mixed layer because of a weaker summer SAM after ~3.4 Ma (Podder et al., 2021). A study from the same eastern equatorial Indian Ocean ODP Site 758 A revealed a thick mixed layer between ~25.6 and 14.7 Ma and a prominent shift in the upper water column structure at ~12.9 Ma, which is interpreted to reflect the onset of SAM wind system, leading to the development of the modern summer SAM current surface circulation in the Indian Ocean (Podder et al., 2024). However, no records are available from the EAS to test how monsoonal atmospheric circulation changes over the northern Indian Ocean might have affected the upper water column structure in the EAS during the middle Miocene.

For that reason, the objective of this study is to reconstruct changes of the upper water column structure at Site NGHP-01-01 A in the EAS during the middle Miocene. It is thought that the upper part of the water column responds directly to changes in wind strength (e.g., Wyrtki, 1961; Qu et al., 2007). Reconstruction of the oceanic upper surface water structure therefore may represent a sensitive variable of past changes in wind strength. In order to reconstruct the upper surface water column structure, the difference in Mg/Ca-based temperatures (ΔT°C) of surface-dwelling (*Trilobatus sacculifer*), lower mixed layer/thermocline-dwelling (*Dentoglobigerina altispira*), and sub-thermocline-dwelling (*Dentoglobigerina venezuelana*) planktic foraminifera is calculated to estimate the upper ocean thermal gradient. These species are the best choice to reconstruct changes of the upper water column structure at Site NGHP-01-01 A in the EAS during the middle Miocene. *Trilobatus sacculifer* is a mixed layer environment species (Fairbanks et al., 1980, 1982; Erez and Honjo, 1981; Hemleben et al., 1989), which is inhabiting the upper 40 m in the Arabian Sea where the water column is well stratified (Schiebel et al., 2004). Combined shell stable oxygen isotope and Mg/Ca ratios-based habitat depth estimates from the eastern Indian Ocean suggest that *T. sacculifer* calcifies within the mixed layer between 20 m and 50 m (Mohtadi et al., 2011). *Dentoglobigerina altispira* is an extinct planktic foraminifera species and shell $\delta^{18}O$-derived habitat estimates show that *D. altispira* inhabited the lower mixed layer and/or upper thermocline in the EAS during the middle Miocene (Zou et al., 2022). *Dentoglobigerina venezuelana* is also an extinct species and its stable carbon and oxygen isotope data suggest a deep dwelling, sub-thermocline habitat (e.g., Gaspari and Kennett, 1993; Pearson and Shackleton, 1995; Pearson et al., 1997; Pearson and Wade, 2009; Karas et al., 2009).

The differences in Mg/Ca-based temperatures (ΔT°C) between surface-dwelling, thermocline and sub-thermocline-dwelling planktic foraminifera are a common approach for reconstructing the upper water column structure, and a qualitative estimate for the state of the upper ocean thermal gradient (e.g., Steinke et al., 2010, 2011; Mohtadi et al., 2011). The ΔT(°C) between shallow-dwelling species and thermocline/sub-thermocline-dwelling species is usually large when the thermocline is shallow and the mixed layer is reduced, and a large temperature range exists within the photic zone (e.g., Mohtadi et al., 2011). In contrast, a smaller ΔT°C between shallow-dwelling species and subsurface dwelling species indicates a lower temperature gradient and hence a deeper thermocline and a deeper mixed layer depth (MLD), with a narrow temperature range within the photic zone (e.g., Steinke et al., 2010; Mohtadi et al., 2011).

2. Modern oceanography and hydrography

The climate and oceanography of the Arabian Sea are primarily controlled by the seasonally reversing SAM. The summer monsoon brings most of the rainfall to the Indian subcontinent (Webster et al., 1998; Gadgil, 2003). The SAM is driven by the cross-equatorial pressure gradient between the Indian Low and the Mascarene High in the southern Indian Ocean (e.g., Tomas and Webster, 1997; Webster and Fasullo, 2003). The Indian Low is controlled both by direct heating on the Asian continent and the subsequent hidden heat release from moisture from the Indian Ocean (Webster and Fasullo, 2003) and creates an ocean–land–atmosphere interaction and thus acts as a main driving force of hydroclimate in the tropical Indian Ocean. The Mascarene High is controlled by the declining branch of the Hadley cell in the southern hemisphere because of the temperature gradient between the equator and Antarctica (Xue et al., 2004). For that reason, wet laden air flows from the colder Indian Ocean (high atmospheric pressure) to the warmer India subcontinent (low atmospheric pressure), which is also associated with a northern shift of the Inter-Tropical Convergence Zone (ITCZ). Nearly 80% of annual rainfall in India occurs in the summer or southwest (SW) monsoon season (June to September; Fig. 1b; Parthasarathy and Dhar, 1974). The southwest summer monsoon wet winds affect the westcoast of India by end of May or beginning of June each year due to sudden changes in the lower troposphere over the Indian Ocean, which increase the southeast trade winds, resulting in a transverse equatorial flow of trade winds and, consequently, a lower level of the Somali or Findlater Jet (Findlater, 1969). High rainfall on the westcoast of India and river runoff from the Western Ghats via the Narmada and the Tapti rivers and several smaller rivers (e.g., Kalinadi, Gangavati, Sharavati, Periyar, Valapattam, Bharathpuzha, Pamba, and Netravati; Milliman and Farnsworth, 2011) result in an increased supply of freshwater and the development of low-salinity surface waters off the western coast of India (Fig. 1b) during the summer monsoon season at the core location of Site NGHP-01-01 A in the EAS. The sea surface salinity (SSS) of the EAS, therefore, decreases progressively from June to September by 0.5 to 1 psu (Behara et al., 2019). During the winter monsoon season, the gradient of atmospheric pressure changes and the ITCZ shifts south, resulting in a dominant air flow from the colder continent to the warmer ocean. This causes strong, dry, northeastern winds coming from India

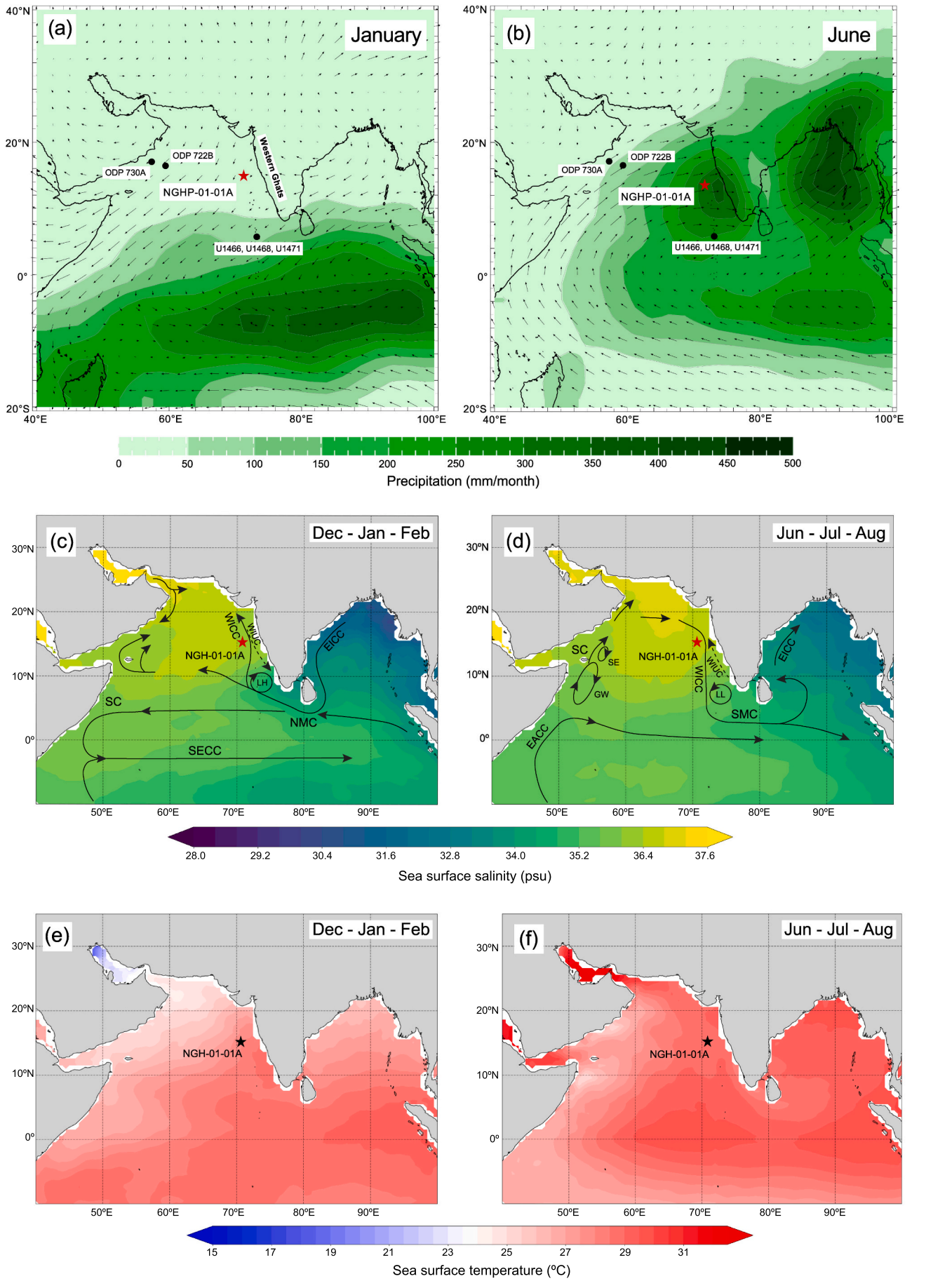

(caption on next page)

Fig. 1. (a and b) Maps of precipitation and surface wind direction, and strength over the northern Indian Ocean for (a) January (winter NE monsoon) and (b) June (summer SW monsoon). The location of marine sediment core NGHP-01-01 A (2006 Indian National Gas Hydrate Program Expedition-01; Collett et al., 2007) is given in a-f. Locations of other cores discussed in this study are indicated in a-b: IODP Expedition Sites U1466, U1468, and U1471, Betzler et al. (2016); ODP Site 730 A, Gupta et al. (2015) and Zhuang et al. (2017); ODP Site 722B (Kroon et al., 1991), Zhuang et al. (2017), and Bialik et al. (2020). Monthly precipitation and surface wind speed and strength for the 925 hPa pressure level are derived from National Centers for Environmental Prediction (NCEP) reanalysis (http://iridl.ledeo.columbia.edu). **(c and d)** Surface water salinity and surface ocean circulation (black lines; according to Schott and McCreary Jr (2001) in the northern Indian Ocean in (c) December–January-February (winter NE monsoon) and (d) June–July-August (summer SW monsoon); SMC, Southwest Monsoon Current; NMC, Northwest Monsoon Current; WICC, West India Coastal Current; WIUC, West India Undercurrent; EICC, East India Coastal Current; SC, Somali Current; SECC, South Equatorial Countercurrent; EACC, East African Current; LH, Laccadive High, LL, Laccadive Low; GW, Great Whirl; SE, Socotra Eddy. The salinity data are from the Institute of Atmospheric Physics (IAP), Chinese Academy of Sciences (CAS) global ocean salinity 0.5° gridded dataset (Li et al., 2023; http://www.ocean.iap.ac.cn). **(d and e)** Sea surface temperature in the northern Indian Ocean in (e) December–January-February (winter NE monsoon) and (f) June–July-August (summer SW monsoon). The sea surface temperature data is from the Institute of Atmospheric Physics (IAP), Chinese Academy of Sciences (CAS) global ocean temperature 0.5° gridded dataset (Li et al., 2023).

and flowing towards the Arabian Sea with excessive evaporation over precipitation and net thermal losses from the ocean (e.g., Gadgil, 2003).

During the summer monsoon season, a clockwise surface water circulation develops in the Arabian Sea (Schott and McCreary Jr, 2001). The eastern branch of this anticyclonic circulation forms the West India Coastal Current (WICC; Shetye et al., 1991) in the EAS. The southward-flowing WICC in summer carries high-salinity waters from the northern Arabian Sea towards the south (Prasanna Kumar et al., 2004), leading to slightly higher salinity along the west coast of India (Prasanna Kumar et al., 2004; Fig. 1d), while the West India Undercurrent (WIUC) moves northward and extends up to 17°N and to a depth of ~200 m (Shetye et al., 1990; Antony, 1990; Muraleedharan et al., 1995). The WIUC carries low saline and more oxygenated water and is about 40 km wide with its core at 150 m in the southern part and deepens in the north with its core ~250 m (off Goa) (Shetye et al., 1990; Naqvi et al., 2006).

During the winter monsoon season when the wind system reverses, the WICC flows northward and transports low salinity waters from the Bay of Bengal (BoB) into the EAS extending up to a depth of ~150 m (Prasanna Kumar et al., 2004). This low-salinity BoB water is carried by the southward flowing East Indian Coastal Current (EICC) and then fed into the WICC (e.g., Prasanna Kumar et al., 2004; Fig. 1c). In the southeastern Arabian Sea, SSS decreases by about 1.5 psu during winter (Behara et al., 2019). The WIUC flows southward during the winter monsoon season (Shetye et al., 1990).

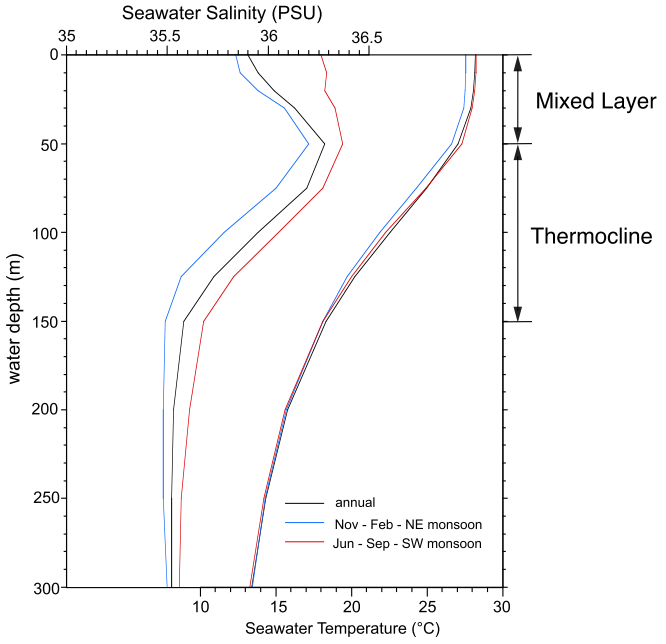

Fig. 2. Salinity and temperature profiles at Site NGHP-01-01 A for annual (black line), November–February (NE monsoon season; blue line) and June to September (red line). Please note that the seasonal temperature and salinity profiles at Site NGHP-01-01 A do not reveal any significant differences in mixed layer depth (MLD; ~50 m water depth) during both seasons. Salinity and temperature profiles are from the World Ocean Atlas 2009 (WOA09; Antonov et al., 2010; Locarnini et al., 2010). (For interpretation of the references to colour in this figure legend, the reader is referred to the web version of this article.)

Modern observations show that the seasonally reversing winds also modulate the mixed layer depth (MLD) in the EAS (e.g., Burkill et al., 1993). In the central EAS, the MLD in winter is reported to be slightly deeper (60–80 m) than during the summer (40–80 m) (Rao et al., 1989; Madhupratap et al., 1996). Although the temperature of the mixed layer is slightly lower (~27.3 °C) during the winter monsoon season than during the summer monsoon season (~28 °C), seasonal temperature and salinity profiles at Site NGHP-01-01 A do not reveal any significant differences in mixed layer depth (~50 m water depth) during both seasons (World Ocean Atlas, WOA 2009; Antonov et al., 2010; Locarnini et al., 2010; Fig. 1e and f; Fig. 2). A recent observational study from the central EAS shows a MLD of 38 ± 21 m and depths of 26 °C isotherm (= top of the thermocline in the EAS) of 99 ± 12 m during the peak winter SAM (January) and a slightly shallower MLD of 23 ± 22 m and depths of 26 °C isotherm of 36 ± 25 m during the peak summer SAM (August) (Sherin et al., 2023). A prominent MLD deepening in the south of the EAS during winter SAM season is inhibited due to advection of low-salinity water carried by the northward-flowing WICC (Shankar et al., 2016; Vijith et al., 2016; Fig. 1c).

In the southeastern Arabian Sea (SEAS), a 20 m thick barrier layer (BL) exists during March–April because of the advection of a surface layer of low-salinity waters from the Bay of Bengal (BoB) during December–January (Shenoi et al., 2004). The BL is almost annihilated by April–May due to the onset of upwelling, and by the advection of higher-salinity waters from the north and by mixing due to stronger winds, which deepen the mixed layer in the SEAS (e.g., Durand et al., 2004; Shenoi et al., 2004).

3. Materials and methods

3.1. Site description and age model

During the National Gas Hydrate Program (NGHP) cruise in 2006, Site NGHP-01-01 A was recovered by the drill ship JOIDES Resolution (JR) in the Kerala-Konkan Basin in the Eastern Arabian Sea (15°18.366′ N, 70°54.192′ E; 2663 m water depth; Collett et al., 2007, Fig. 1). The age model for the investigated middle Miocene time interval (16–11 Ma; depth interval 212–172 mbsf) is based on orbital tuning of the bulk density measurements acquired by wireline logging (Collett et al., 2007). A detailed description about the refined age model can be found in Yang et al. (2020). The age control points used to construct the age model for Site NGHP-01-01 A in the depth interval 212–172 mbsf (~16–11 Ma) (Yang et al., 2020) are given in the supporting information (Table S1).

3.2. Samples, sample preparation and additional datasets

The difference in Mg/Ca-based temperatures (ΔT°C) between surface-dwelling (*T. sacculifer*) and thermocline-dwelling (*D. altispira*) and sub-thermocline-dwelling (*D. venezuelana*) planktic foraminifera was estimated to reconstruct the upper water column structure at Site NGHP-01-01 A. A total of 106 samples were analyzed for *D. venezuelana* stable oxygen isotopes and 201 samples for trace elements between ~185–210 m below seafloor (mbsf) of Site NGHP-01-01 A. In order to allow a comparison within the same sample, the sample resolution of the *T. sacculifer* $\delta^{18}O$ and Mg/Ca-SST records of Site NGHP-01-01 A as previously published in Yang et al. (2020) were increased for this study. An additional 388 and 138 samples for stable oxygen isotopes and trace elements on *T. sacculifer* have been analyzed for this study, respectively. All samples were freeze dried, wet-sieved over a 63 μm and a 150 μm sieve and oven-dried at 55 °C. Thereafter, *D. venezuelana* and *T. sacculifer* specimens were picked out of the samples with a brush for oxygen isotope and trace element analyses. The isotope and trace element data for the planktic foraminifera *D. altispira* and the difference of the Mg/Ca-based temperatures (ΔT°C) between surface-dwelling planktic foraminiferal species *T. sacculifer* and thermocline-dwelling *D. altispira* have been previously published in Zou et al. (2022).

3.3. Planktic foraminiferal stable oxygen isotopes

Stable oxygen isotopes were measured on samples composed of ~5–10 *D. venezuelana* specimens of the 315–355 μm size fraction and ~ 5–15 *T. sacculifer* specimens of the 250–355 μm size fraction. The isotopic composition of the planktic foraminifera samples was analyzed at the MARUM, University of Bremen, Germany, using a Finnigan MAT 251 mass spectrometer equipped with an automatic line for carbonate preparation (type "Kiel III"). Data are reported in the usual delta-notation versus V-PDB. The instrument was calibrated against the house standard (ground Solnhofen limestone), which in turn was calibrated against the internationally distributed reference material NBS (National Bureau of Standards, USA) 19 calcite. The average standard deviation of the in-house standard was ±0.05‰ for $\delta^{18}O$ over the measurement period.

3.4. Planktic foraminiferal trace element analyses

For the analysis of planktic foraminiferal trace elements, we analyzed ~20–30 *D. venezuelana* specimens of the 315–355 μm size fraction and ~ 30 *T. sacculifer* specimens of the 250–355 μm size fraction. The cleaning protocol for planktic foraminiferal trace element analyses of Barker et al. (2003) was used to clean the planktic foraminiferal tests prior to the elemental analyses. As part of the cleaning process, the tests were crushed, ultrasonicated and rinsed several times to remove clay minerals, organic matter was removed by oxidation, and any remaining contaminants were removed by acid leaching. After the shell fragments were dissolved, the samples were centrifuged at 6000 rpm for 10 min. Trace element concentrations were measured using an Inductively Coupled Plasma Optical Emission Spectrophotometer (ICP-OES; Agilent 5110 VDV) at the Center of Major Equipment and Technology (COMET) of the State Key Laboratory of Marine Environmental Science (MEL), Xiamen University. The Mg/Ca values are reported as mmol/mol. After every five samples an in-house standard (Mg/Ca = 4.12 mmol/mol) was measured to examine the instrumental precision. The relative standard deviation of the in-house standard was 0.02 mmol/mol for Mg/Ca. Replicate measurements of re-picked *D. altispira* samples ($n = 81$) and *T. sacculifer* ($n = 29$) samples revealed an average standard deviation for Mg/Ca of 0.18 mmol/mol and 0.15 mmol/mol, respectively. Al/Ca, Mn/Ca and Fe/Ca were determined along with Mg/Ca to assess the efficiency of the cleaning process, i.e., the removal of clays and the occurrence of *syn*-sedimentary and post-depositional precipitated Fe-Mn-oxyhydroxides and Fe—Mn carbonate coatings, respectively (see below).

3.5. Mg/Ca temperatures estimates

We note that *D. venezuelana* is an extinct species and therefore no species-specific Mg/Ca-temperature calibration exists for this species. Assuming that *D. venezuelana* incorporates Mg into its test similarly as modern planktic foraminiferal species, we used the multiple species planktic foraminifera calibration of Anand et al. (2003):

$$\mathrm{Mg/Ca\ (mmol/mol)} = 0.38\ exp.(0.090 \times \mathrm{T\ (^{\circ}C)} \quad (1)$$

to convert the *D. venezuelana* Mg/Ca ratios to temperature. The errors of the temperature estimates were calculated according to the approach of Mohtadi et al. (2014), which includes a propagation of the errors introduced by the Mg/Ca measurements and the Mg/Ca-temperature calibration (see Mohtadi et al., 2014, for details). The resulting (1σ) errors are on average 1.0 °C for the *D. venezuelana* temperature estimates. Mixed layer temperature (°C) estimates based on *T. sacculifer* were obtained by using the same multiple species planktic foraminifera calibration species-specific equation (Anand et al., 2003; see above). The (1σ) errors are on average 1.2 °C for the SST estimates. Because seawater Mg/Ca has been shown not to be constant over time (e.g., Evans and Müller, 2012; Stanley and Hardie, 1998; Evans et al., 2016), palaeo-Mg/Ca temperature records on such long-time scales may require a correction for secular changes in seawater Mg/Ca. A record of seawater Mg/Ca estimates derived from fluid inclusion, calcite vein and echinoderm proxies (Lear et al., 2015) was used to correct the planktic foraminiferal shell Mg/Ca for changes in seawater Mg/Ca:

$$\mathrm{Seawater\ Mg/Ca\ (mol/mol)} = 5.2 - (0.238^{*}\mathrm{age}) + (0.00661^{*}\mathrm{age}^{2}) - (6.66e^{-5^{*}}\mathrm{age}^{3}) \quad (2)$$

To account for past seawater Mg/Ca changes, the *D. venezuelana* and *T. sacculifer* Mg/Ca estimates were adjusted for changes in seawater Mg/Ca by modifying the Mg/Ca-temperature calibrations of Anand et al. (2003; see above), following Lear et al. (2015):

$$\mathrm{T\ (^{\circ}C)} = \ln \mathrm{Mg/Ca} \ln \mathrm{Mg/Ca_{Miocne-sw}/Mg/Ca_{Modern-sw}} - ln\ 0.38)/0.09) \quad (3)$$

where Mg/Ca is the measured planktic foraminiferal Mg/Ca in mmol/mol, $\mathrm{Mg/Ca_{Miocene\text{-}sw}}$ the Miocene Mg/Ca seawater, which was calculated following the eq. (2) and $\mathrm{Mg/Ca_{Modern\text{-}sw}}$ the modern seawater Mg/Ca, which is 5.1 mol/mol at present (Broecker and Peng, 1982; Wilkinson and Algeo, 1989).

3.6. Seawater $\delta^{18}O$ estimates

Combining the measured shell Mg/Ca and stable oxygen isotopes of *D. venezuelana* (this study), *D altispira* (Zou et al., 2022) and *T. sacculifer* (Yang et al., 2020; this study) allows to reconstruct seawater $\delta^{18}O$ variations, which provides information about the salinity of the sub-thermocline and mixed layer waters. Changes in seawater $\delta^{18}O$ ($\delta^{18}O_{sw}$) were calculated using the unadjusted and adjusted temperature Mg/Ca-temperature estimates in order to account for past seawater Mg/Ca changes by removing the temperature-driven component of the planktic foraminifera $\delta^{18}O$ record. The $\delta^{18}O$-temperature relationship of (Bemis et al., 1998) was then used to calculate the $\delta^{18}O_{sw}$ estimates:

$$\delta^{18}O_{sw}\ (\mathrm{SMOW‰}) = \left(\mathrm{T(^{\circ}C)} - 16.5 + 4.8 \times \delta^{18}O_{calcite}\ (\mathrm{VPDB)‰}\right)/4.8 + 0.27 \quad (4)$$

The values were converted to standard mean ocean water (SMOW) by adding 0.27%. A local record of changes in $\delta^{18}O_{sw}$ (i.e., proxy for local changes in salinity) was derived by subtracting an estimate of middle Miocene ice-volume changes from the $\delta^{18}O_{sw}$ record. The benthic foraminiferal stable oxygen isotope record of Ocean Drilling Program (ODP) Site 1146 located in the northern South China Sea (Holbourn et al., 2018) was used to derive an estimate of ice volume

changes for the middle Miocene. According to Shevenell et al. (2008), ~70% of the benthic foraminiferal oxygen isotope signal in the middle Miocene is due to changes in continental ice volume. After normalizing the benthic foraminifera record at ODP Site 1146 to its average value and subtracting 70% of the benthic foraminifera record, the local $\delta^{18}O_{sw}$ values were calculated, which provide approximate values of the relative changes in upper water salinity during the middle Miocene (see Steinke et al., 2010; Yang et al., 2020). The errors of the $\delta^{18}O_{sw}$ values are calculated by propagating the error introduced by the planktic foraminiferal $\delta^{18}O$ and Mg/Ca measurements, the Mg/Ca-temperature calibration, and the $\delta^{18}O$-temperature relationship. The resulting errors (1σ) for the $\delta^{18}O_{sw}$ are ~0.22‰ for *D. venezuelana*, ~0.18‰ for *D. altispira*, and ~ 0.24‰ for *T. sacculifer*.

3.7. Statistical transition point estimation

In order to quantify the onset of transitions in our ΔT°C and seawater $\delta^{18}O$ records, we fitted continuous piecewise regression lines with a single breakpoint through our ΔT°C and seawater $\delta^{18}O$ records, using the R package "segmented" (Muggeo, 2008).

4. Results

4.1. The potential influence of contaminations on the planktic foraminiferal test Mg/Ca

Fe/Ca and Al/Ca were analyzed along with Mg/Ca to assess possible contamination by clay minerals. Mn/Ca and Fe/Ca ratios were

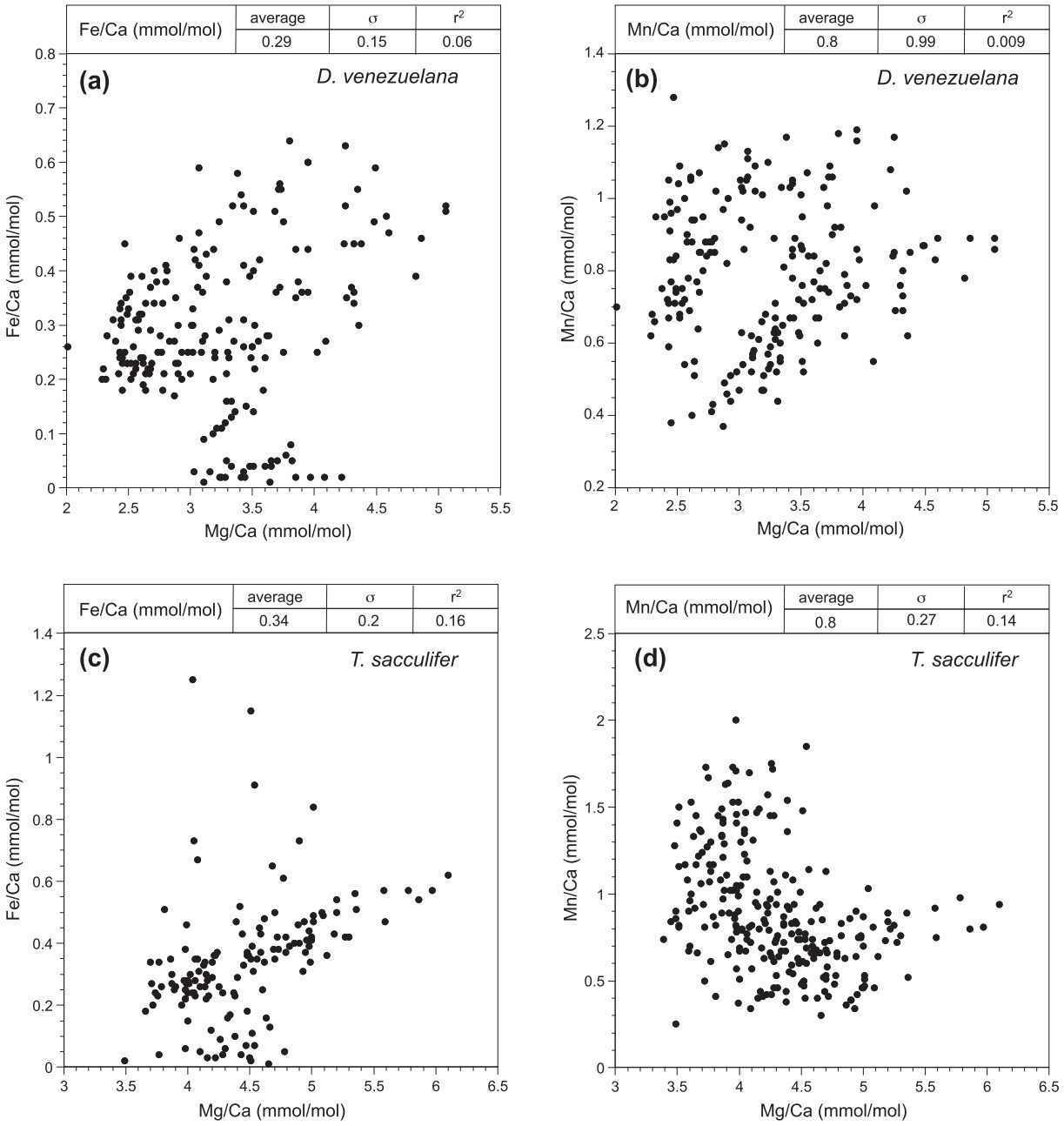

Fig. 3. *Dentoglobigerina venezuelana* Mg/Ca of Site NGHP-01-01 A compared to Fe/Ca **(a)** and Mn/Ca **(b)** for the time interval ~ 16 Ma to 11 Ma. *Trilobatus sacculifer* Mg/Ca plotted versus Fe/Ca **(c)** and Mn/Ca **(d)** for the same site and time interval. No correlation between Mg/Ca and Fe/Ca and between Mg/Ca and Mn/Ca of the *D. venezuelana* samples and only a very low correlation between Mg/Ca and Fe/Ca and between Mg/Ca and Mn/Ca for the *T. sacculifer* samples suggests that the Mg/Ca analyses are not affected by Fe—Mn contaminates.

monitored as an indicator of Fe-Mn-oxyhydroxides and Fe—Mn carbonate coatings (e.g., Boyle and Keigwin, 1985). It has been noted by Barker et al. (2003) that planktic foraminiferal test Mg/Ca may be contaminated when the Mn/Ca and Fe/Ca are higher than 0.1 mmol/mol. The *D. venezuelana* Mn/Ca and Fe/Ca values varied between 0.36 and 1.24 mmol/mol and 0.01 and 0.67 mmol/mol for *D. venezuelana*, respectively. Mn/Ca and Fe/Ca values of the *T. sacculifer*, samples varied between 0.25 and 1.63 mmol/mol and 0.01 and 1.25 mmol/mol, respectively (Fig. 3). Most of these Mn/Ca and Fe/Ca values are higher than the 0.1 mmol/mol Mn/Ca and Fe/Ca ratios given by Barker et al. (2003) for clean, uncontaminated foraminiferal tests. Although high Fe/Ca (up to 0.67 mmol/mol in *D. venezuelana* and 1.25 mmol/mol in *T. sacculifer*) were found, we assume that the Mg/Ca analyses were not contaminated by clay particles because Al was not detected by using ICP-OES technique. Alternatively, the high Fe/Ca and Mn/Ca might be related to the presence of Fe-Mn-oxyhydroxides and/or Fe-Mn-carbonates on the planktic foraminiferal tests, which might result in elevated Mg/Ca. Although the Mn/Ca and Fe/Ca ratios are higher than the 0.1 mmol /mol for uncontaminated samples, there exists no relationship ($r^2 = 0.06$) between Mg/Ca and Fe/Ca and between Mg/Ca and Mn/Ca ($r^2 = 0.009$) of the *D. venezuelana* samples and only a very low correlation between Mg/Ca and Fe/Ca ($r^2 = 0.16$) and Mg/Ca and Mn/Ca ($r^2 = 0.14$) for the *T. sacculifer* samples (Fig. 3). Those results argue against a significant influence of *syn*-sedimentary and post-depositionally precipitated Fe-Mn-oxyhydroxides and/or Fe-Mn-rich carbonate coatings and indicate that the Mg/Ca analyses are not affected by Fe—Mn contaminates.

4.2. Stable oxygen isotopes

The $\delta^{18}O$ values of *D. venezuelana* vary between −0.64‰ and 1.39‰ during the time interval ~ 15.8 Ma and 12.5 Ma (Fig. 4a). The $\delta^{18}O$ values are relatively constant between ~15.8 Ma and 14.2 Ma, followed by an increase in $\delta^{18}O$ from ~14.2 Ma to 12.5 Ma. The trend of $\delta^{18}O$ values of the *D. venezuelana* is opposite to the trends of the $\delta^{18}O$ records for *T. sacculifer* (this study, Yang et al., 2020) and *D. altispira* (Zou et al., 2022) from the same core, which reveal a decrease in $\delta^{18}O$ after ~14.2 Ma (Fig. 4a). The $\delta^{18}O$ values of *T. sacculifer* vary between −1.01‰ and − 3.51‰ between ~15.8 and 11 Ma (Fig. 4a). Different to the *D. venezuelana* $\delta^{18}O$ record, the $\delta^{18}O$ record of *T. sacculifer* shows a long-term gradual decrease in $\delta^{18}O$ from ~15.8 and 11 Ma (Fig. 4a).

4.3. Mg/Ca-temperature estimates

The *D. venezuelana* Mg/Ca of Site NGHP-01-01 A vary between 2.01 and 4.82 mmol/mol during the time interval ~ 15.8–12.5 Ma (Fig. 4b). The estimated temperatures for the sub-thermocline calculated from Mg/Ca of *D. venezuelana* reveal that the temperature during this period varied between ~18.5 °C and 28.2 °C (Fig. 4c). Highest temperatures occur between ~15.8 Ma and ~ 14.2 Ma with an average value of ~25.3 °C, except for a brief cooling of ~23 °C from ~14.4 Ma to 14.6 Ma. The sub-thermocline temperatures reveal a prominent decrease after ~14.2 Ma during the MMCT. The *T. sacculifer* Mg/Ca ratios vary between 3.39 and 6.10 mmol/mol (Fig. 4b). Changes in sea surface water temperatures as deduced from the *T. sacculifer* Mg/Ca SST estimates are similar to the temperature evolution of the sub-thermocline (Fig. 4c). Higher temperatures between ~15.8 Ma and ~ 14.2 Ma with an average value of ~27.5 °C are followed by a distinct decrease in SST at around 14.2 Ma (Fig. 4c). After the distinct decrease in SSTs, relatively constant SSTs of around 26.1 °C occurred between ~14 Ma to 11 Ma (Fig. 4c). The adjusted Mg/Ca temperature estimates of *D. venezuelana* and *T. sacculifer* for changes in seawater Mg/Ca results are on average 6 °C higher than those estimated without a correction for changes in seawater Mg/Ca (Fig. 4d). Despite the fact that the absolute Mg/Ca-based temperature estimates may be affected by temporal variations in seawater Mg/Ca during the middle Miocene, it is suggested that the amplitude, trend, and timing of the surface and sub-thermocline water temperature changes are not affected as shown by the approach to account for past seawater Mg/Ca changes (Fig. 4d). We therefore suggest that those changes in the surface and sub-thermocline water temperatures can be used to estimate changes in EAS surface and sub-thermocline water temperatures during the middle Miocene.

4.4. Local $\delta^{18}O$ of seawater

The local $\delta^{18}O_{sw}$ reconstructions using the Mg/Ca-based sub-thermocline temperature estimates reveal values varying between ~3.12 ‰ and 0.79‰ during the time interval ~ 15.8–12.5 Ma (Fig. 4e). The local *D. venezuelana* based $\delta^{18}O_{sw}$ estimates reveal a prominent shift towards lower (lighter) local $\delta^{18}O_{sw}$ values after ~14.4 Ma, indicating a freshening of the sub-thermocline waters in the EAS. The mixed-layer/surface water *T. sacculifer* based local $\delta^{18}O_{sw}$ estimates vary between 2.07‰ and − 1.24‰ during the time interval ~ 15.8 Ma and 11 Ma (Fig. 4e). The local *T. sacculifer* (this study; Yang et al., 2020) and *D. altispira* (Zou et al., 2022) based $\delta^{18}O_{sw}$ estimates reveal the same freshening after ~14.3 Ma of the upper and lower mixed layer/upper thermocline waters as inferred from $\delta^{18}O_{sw}$ estimates based on Mg/Ca and oxygen isotopes of *D. venezuelana,* respectively, from the same core (Fig. 4e). Determination of breakpoints in the local $\delta^{18}O_{sw}$ estimates of *D. venezuelana* using the R package "segmented" (Muggeo, 2008; Figs. 4e) indicates breakpoints at 15.12 ± 0.23 Ma (1σ) and 13.02 ± 0.16 Ma, which are significant when compared by F test to a model with no breakpoints ($F = 5.62$, $p < 0.001$). The local $\delta^{18}O_{sw}$ record of *T. sacculifer* reveals a pair of breakpoints at 14.38 ± 0.05 Ma (1σ) and 14.04 ± 0.61 Ma, which are highly significant. No breakpoints are detected in the local $\delta^{18}O_{sw}$ record of *D. altispira*, which might be related to the low resolution compared to the $\delta^{18}O_{sw}$ records of *D. venezuelana* and *T. sacculifer*. The local seawater $\delta^{18}O$ estimates of all three species using Mg/Ca-based temperatures adjusted for changes in seawater Mg/Ca are on average 1.3‰ heavier than those calculated with unadjusted Mg/Ca-based temperatures (Fig. 4f). Although the absolute local $\delta^{18}O_{sw}$ values are different, the trends and timing of both approaches (using unadjusted vs. adjusted Mg/Ca-based SST estimates) are identical (Figs. 4f and 4 g). We therefore think that the changes in the local $\delta^{18}O_{sw}$ estimates can give us a good idea of relative changes in local mixed layer and sub-thermocline $\delta^{18}O_{sw}$ in the EAS during the middle to late Miocene.

4.5. Thermal gradient (ΔT) estimates

The ΔT reconstructions using the mixed layer dweller *T. sacculifer* and sub-thermocline dweller *D. venezuelana* reveal a generally smaller (~2.9 °C) thermal gradient between the surface and sub-thermocline waters between ~15.8 Ma and 14.2 Ma (Fig. 5a), except for the period 14.8–14.6 Ma with a prominent higher (~5.4 °C) thermal gradient between the surface and sub-thermocline waters. The $\Delta T_{(T.\ sacculifer\ -\ D.\ venezuelana)}$ estimates show an overall increase after ~14.3 Ma, indicating a weaker mixing and a better stratification in the EAS after ~14.2 Ma. The thermal gradient (ΔT°C) estimates between the mixed layer and lower mixed layer/upper thermocline ($\Delta T_{(T.\ sacculifer\ -\ D.\ altispira)}$) reveal the same trend with a smaller gradient between the surface and lower mixed layer/upper thermocline between ~15.8 Ma and 14.2 Ma and an overall increase in ΔT thereafter (Fig. 5a), indicating a weaker mixing and a better stratification in the surface waters of the EAS after ~14.2 Ma. Determination of breakpoints of the thermal gradient (ΔT°C) estimates reveal breakpoints for the $\Delta T_{(T.\ sacculifer\ -\ D.\ venezuelana)}$ record at 14.24 ± 0.19 Ma (1σ) and 14.02 ± 0.15 Ma and for the $\Delta T_{(T.\ sacculifer\ -\ D.\ altispira)}$ record at 14.13 ± 0.21 Ma (1σ) and 13.9 ± 0.52 Ma, which are however statistically not significant (Fig. 5a).

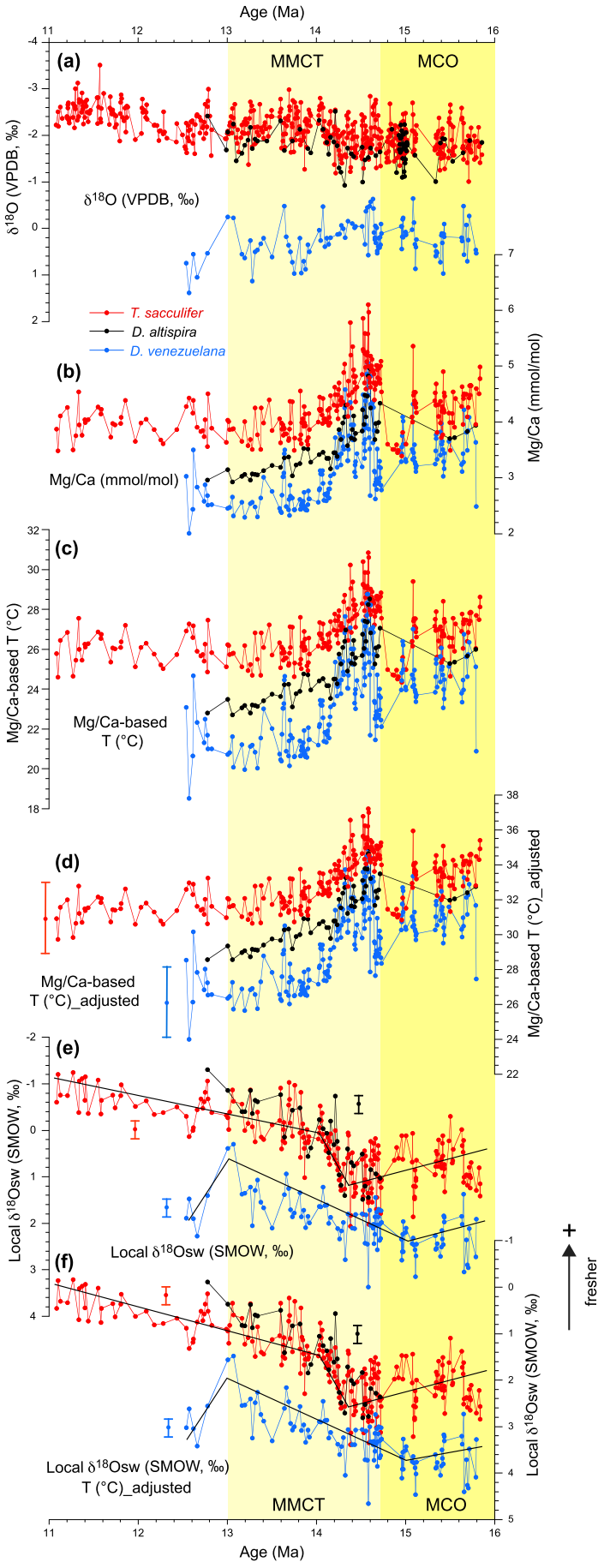

(caption on next page)

Fig. 4. **(a)** Oxygen isotope records of *Trilobatus sacculifer* (red; this study, Yang et al., 2020), *Dentoglobigerina altispira* (black; Zou et al., 2022), and *Dentoglobigerina venezuelana* (blue; this study) of Site NGHP-01-01A, **(b)** Mg/Ca ratios (mmol/mol) of *T. sacculifer* (red; this study, Yang et al., 2020), *D. altispira* (black; Zou et al., 2022), and *D. venezuelana* (blue; this study). **(c)** Mg/Ca temperature estimates (°C) for *T. sacculifer* (red; this study, Yang et al., 2020), *D. altispira* (black; Zou et al., 2022), and *D. venezuelana* (blue; this study). **(d)** Mg/Ca temperature estimates of the three planktic foraminiferal species corrected for changes in seawater Mg/Ca. **(e-f)** Local seawater $\delta^{18}O$ estimates at NGHP-01-01A for all three planktic foraminiferal species. Black lines in (e-f) indicate the statistical breakpoints analyses (see text for details). Bars in (d) and (e-f) indicate 1σ errors. Yellow vertical bars indicate the Miocene Climatic Optimum (MCO) and the Middle Miocene climate transition (MMCT). (For interpretation of the references to color in this figure legend, the reader is referred to the web version of this article.)

5. Discussion

5.1. Sub-thermocline temperature and salinity changes

The major feature of the sub-thermocline temperature record at Site NGHP-01-01 A is a distinct cooling between ~14.2 Ma and 13.2 Ma in the EAS (Fig. 4c). The sub-thermocline cooled by ~8 °C during this period. A similar temperature trend is also observed in the upper mixed layer (Yang et al., 2020) and in the lower mixed layer/upper thermocline (Zou et al., 2022) with a decrease in temperature of ~4 °C and ~ 6 °C during the MMCT, respectively (Figs. 4c; 6a). This prominent decrease in sub-thermocline temperature is associated with a freshening of the sub-thermocline as inferred from the local *D. venezuelana* based $\delta^{18}O_{sw}$ estimates which reveal a prominent shift towards lower (lighter) local $\delta^{18}O_{sw}$ values and thus lower salinity (Figs. 4e and 6b). The cooling and freshening of the sub-thermocline in the EAS coincide with the shoaling and final closure of the Miocene Indian Ocean Gateway ("Tethyan Seaway") to the Mediterranean at around ~14 Ma (e.g., Hamon et al., 2013; Bialik et al., 2019). The shoaling and final closure of the Miocene Indian Ocean Gateway ceased the inflow of the warm and salty Tethyan Indian Saline Waters (TISW) from the Mediterranean Sea into the Arabian Sea (Bialik et al., 2019). In this context, model simulations show that a shoaling of the Tethyan Seaway to 250 m and its final closure resulted in the termination of TISW production (Hamon et al., 2013). Bialik et al. (2019) suggest that the TISW advection might have affected the whole Arabian Sea and the eastern African Margin. We therefore suggest that the closure of the Tethyan Seaway at around ~14 Ma caused the termination of the inflow of the warm and salty TISW into the Arabian Sea, which likely resulted in a cooling and freshening of the sub-thermocline at Site NGHP-01-01 A in the eastern Arabian Sea. We suggest that the higher density of the TISW may have prevented any impact on the surface waters in our study area similar to the modern Persian Gulf Water (PGW) mass (Prasad et al., 2001). In addition, the final closure of the Tethyan Seaway led to significant changes in the oceanography of the Indian and Southern Ocean. Numerical model simulations suggest that the closure of the Tethyan seaway and the cessation of the advection of the TISW also caused strong changes in the latitudinal density gradient and a strengthening of the Antarctic Circumpolar Current (ACC; Hamon et al., 2013). Prior to the closure of the Tethyan Seaway, the presence of the TISW, which was warm and saline, might have been associated with a slow proto-Antarctic Circumpolar Current (ACC), preventing the expansion of East Antarctic Ice Sheets during the early and early middle Miocene (Woodruff and Savin, 1989; Wright et al., 1992). A strengthened ACC resulted in lower SSTs, an increase in sea ice extent and a stronger latitudinal thermal gradient, and thus a strengthening of the westerlies (Hamon et al., 2013). A strengthening of the ACC is also associated with a gradual cooling and freshening of the surface waters between 14.2 and 13.8 Ma at ODP Site 1171C in the subantarctic Southwest Pacific (Shevenell et al., 2004). The distinct cooling and freshening of the sub-thermocline in the EAS coincide with the cooling and freshening in the ACC region at ODP Site 1171C in the subantarctic Southwest Pacific (Shevenell et al., 2004; Fig. 6 c and d). As discussed previously in Yang et al. (2020), it might be possible that the Southern Ocean Intermediate Waters (SOIW) may have transmitted the changes in temperature and salinity to the Arabian Sea via the "oceanic tunnel" mechanism (Liu and Yang, 2003; Pena et al., 2013), as previously shown for other locations in the Indian Ocean during the Pleistocene and Holocene (e.g., Kiefer et al., 2006; Romahn et al., 2014). After subducting and spreading northward into the Indian Ocean, the SOIW forms the Indian Ocean Central Water (IOCW; You, 1998), which reached the surface waters in the WAS and south-western EAS upwelling regions, likely affecting the hydrography from the sub-thermocline to the surface, resulting in the pronounced decrease in temperature and salinity at Site NGHP-01-01 A (Fig. 6 a and b).

5.2. Upper water column structure

The $\Delta T_{(T.\ sacculifer\text{-}D.\ venezuelana)}$ estimates reveal weaker mixing, a shallower thermocline and a better stratification in the EAS after ~14.2 Ma (Fig. 5a). This is corroborated by the difference in Mg/Ca-based temperatures (ΔT°C) of the surface-dwelling planktic foraminifera *T. sacculifer* and the lower mixed layer/upper thermocline-dwelling planktic foraminifera *D. altispira* estimates (Zou et al., 2022; Fig. 5a), which also suggested less mixing and better stratified surface waters in the EAS after ~14.2 Ma. The decrease in mixing and thus shoaling of the thermocline in the EAS after 14.2 Ma coincides with upwelling in the WAS, possibly driven by a strengthening of the summer SAM winds since ~14.7 Ma (e.g., Zhuang et al., 2017; Auer et al., 2023). The intensification of the summer SAM winds after~14.7 Ma is consistent with the proposed northward movement of the southern Westerlies and the Hadley Cell in the Indian Ocean from the middle to the late Miocene (Groeneveld et al., 2017), resulting in a strengthening of the cross-equatorial Somali Jet during this period (e.g., Bialik et al., 2020). Modern observations from the Indian Ocean have revealed that the thermocline depth becomes shallower (deeper) in the eastern (western) Indian Ocean during strong summer SAM (Krishnan et al., 2006; Swapna et al., 2014; Keerthi et al., 2013). In addition, model simulations have shown that wind strength weakens (increased) in the eastern (western) Indian Ocean during maximum summer SAM periods (Jalihal et al., 2019), which enhances (reduces) surface stratification or thermocline shoaling (deepening). We, therefore, suggest that the shallower thermocline depth in the EAS is most likely due to an intensification of the summer SAM. Like in modern-day oceanographic settings, the thermocline depth became shallower with decreasing SST and sub-thermocline temperature after 14.2 Ma (Fig. 4c, 5a), as Podder et al. (2021) also observed in the eastern equatorial Pacific during the Pliocene-Pleistocene. On the contrary, surface water cooling is suggested to deepen the mixed layer and thermocline by convective mixing (e.g., Mathew et al., 2003). Modern observations from EAS show that convective mixing during the winter SAM leads to surface cooling and a deep mixed layer/ thermocline in the north, whereas intense surface layer stratification is caused by the advection of low saline Bay of Bengal waters by West India Coastal Current (WICC), which inhibits vertical mixing in the south (Shankar et al., 2016). The strengthening of the SAM winds and cooling of the surface waters between ~14.2 Ma and 13.2 Ma are associated with an intensification of SAM rainfall as inferred from continental runoff from the Western Ghats and thus an intensification in monsoonal rainfall in West India and the adjacent EAS (Yang et al., 2020; Fig. 5f and g). We therefore suggest that the increased rainfall and higher river runoff from the Western Ghats resulted in fresher surface waters in the EAS, leading to less dense surface waters and thus to a strong salinity stratification. Although the Indian subcontinent was located somewhat closer to the equator during that time, the global ocean-continent constellation was close to its modern configuration by ~14 Ma (Scotese, 2002). The present-day monsoon-driven surface water circulation patterns existed already during the middle Miocene as suggested by Podder et al. (2024). Podder et al. (2024) have noted a thick mixed layer between ~25.6 and 14.7 Ma and a shoaling of the

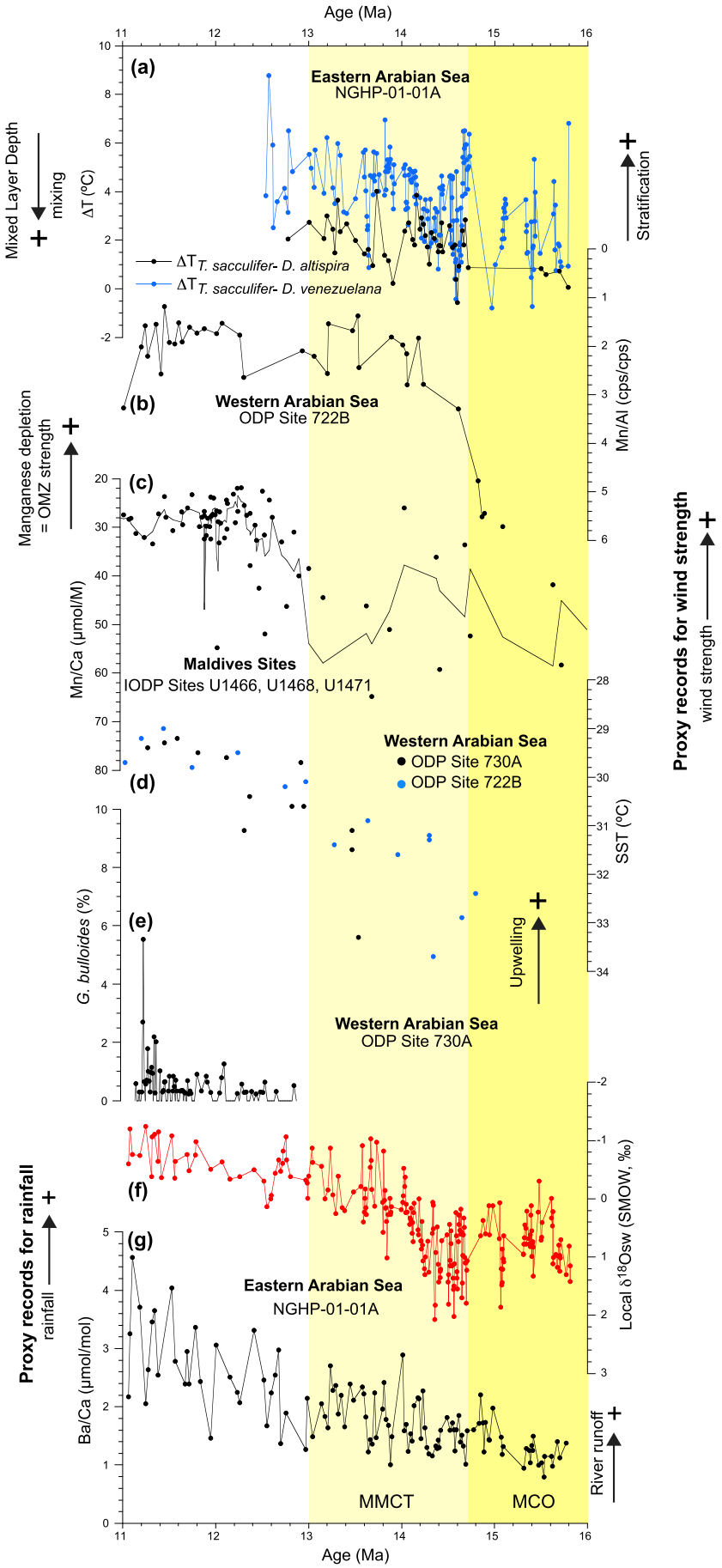

(caption on next page)

Fig. 5. **(a)** $\Delta T_{(T.\ sacculifer\ -\ D.\ venezuelana)}$ (blue) and ($\Delta T_{(T.\ sacculifer\ -\ D.\ altispira)}$) (black) estimates at NGHP-01-01 A compared to other proxy records of changes in the South Asian Monsoon (SAM). **(b)** Mn/Al record of ODP Site 722B from the Western Arabian Sea (Bialik et al., 2020) and **(c)** Mn/Ca record from the Maldives Inner Sea, fluctuations (Betzler et al., 2016; black line: 3-point running average), which are proxy records for Oxygen Minimum Zone (OMZ) fluctuations. **(d)** TEX86 SST estimates of ODP Sites 722B and 730 A from the Western Arabian Sea (Zhuang et al., 2017). **(e)** *G. bulloides* relative abundances of ODP Site 730 A (Gupta et al., 2015) from the Western Arabian Sea. **(f)** *T. sacculifer* based local mixed later seawater $\delta^{18}O$ estimates at NGHP-01-01 A (this study, Yang et al., 2020). **(g)** Ba/Ca ratios of Site NGHP-01-01 A from the Eastern Arabian Sea (Yang et al., 2020). MCO: Miocene Climatic Optimum; MMCT: Middle Miocene climate transition. (For interpretation of the references to colour in this figure legend, the reader is referred to the web version of this article.)

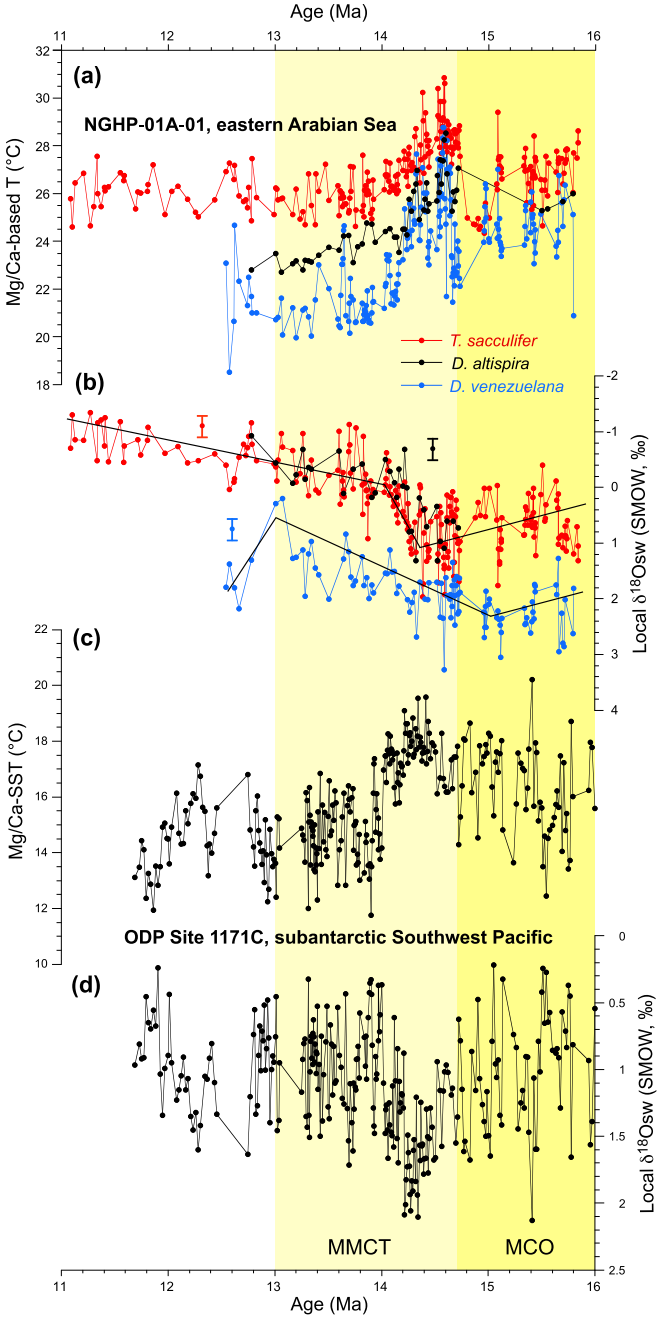

Fig. 6. **(a)** *Trilobatus sacculifer* (red; this study, Yang et al., 2020), *Dentoglobigerina altispira* (black; Zou et al., 2022), and *Dentoglobigerina venezuelana* (blue; this study) Mg/Ca based surface water temperature estimates at Site NGHP-01 A-01. **(b)** Local seawater $\delta^{18}O$ estimates derived from the aforementioned planktic foraminiferal species at NGHP-01-01 A. **(c)** Mg/Ca-based SST estimates and **(d)** seawater $\delta^{18}O$ estimates of ODP Site 1171C from the subantarctic Southwest Pacific (Shevenell et al., 2004). MCO: Miocene Climatic Optimum; MMCT: Middle Miocene climate transition. (For interpretation of the references to colour in this figure legend, the reader is referred to the web version of this article.)

thermocline thereafter with a prominent shift in the in the upper water column structure at ~12.9 Ma, which is interpreted to reflect the onset of SAM wind system, leading to the development of the modern summer SAM current surface circulation in the Indian Ocean (Podder et al., 2024). Like today, we suggest that an intrusion of lower salinity water from the eastern Indian Ocean related to an increased summer runoff of the Ganga-Brahmaputra river system into the Bay of Bengal (BoB) due to a stronger SAM rainfall over the Indian subcontinent and the BoB region during the MMCT contributed to the freshening of the surface waters at Site NGHP-01-01 A. Similar to today, low salinity BoB water might have been carried by the southward flowing EICC and then fed into the WICC flowing northward reducing the salinity in the EAS (see above). Since the stratification is strong under such a scenario, the mixed layer is less reactive to wind anomalies, and the mixed layer would not deepen much. Although the wind patterns over the Arabian Sea are considered to have been strengthened during the MMCT and thereafter (see references above), the proposed strong salinity stratification might have counteracted a deepening of the mixed layer. In analogy to modern hydrography and climatology (see below), it is speculated that under the influence of salinity stratification, resulting from heavy rainfall, river runoff and advection of low salinity waters, the formation of a barrier layer (BL; e.g., Sprintall and Tomczak, 1992; Qu and Meyers, 2005) might have enhanced the salinity stratification, stabilizing a shallow mixed layer in the EAS after ~14.2 Ma. Modern observations show a 20 m thick BL in the southeastern Arabian Sea during March–April because of the advection of low-salinity surface waters during the winter months from the BoB (Shenoi et al., 2004; see above). We therefore suggest that the intensification of the summer SAM rainfall between ~14.8 Ma and 14.0 Ma, which is associated with a higher riverine runoff from the Western Ghats and the advection of low salinity waters from the BoB via the WICC (see above) resulted in the formation of a BL between the bottom of the mixed layer and the top of the thermocline, enhancing the stratification in the EAS after ~14.2 Ma. The advection of scenario, however, cannot yet be fully proven by substantial data sets, especially with regard to the winter SAM development during the middle Miocene. We cannot prove this scenario with independent winter EAM proxy records for the development of the winter EAM during the middle Miocene. Beasley et al. (2021) have found an increase in water column ventilation and water mass mixing between 23.7 and 23.0 Ma, indicating an increase in winter monsoon type atmospheric circulation. It could therefore be possible that with the strengthening of the summer SAM atmospheric and surface ocean circulation during the MMCT, a simultaneous strengthening/intensification of the winter SAM monsoon took place. In addition, the global ocean-continent constellation was close to its modern configuration by ~14 Ma (Scotese, 2002) and a closed Tethyan Seaway by that time, might have allowed also the establishment of a winter EAM circulation in the northern Indian Ocean. In summary, the change in the upper ocean hydrography after ~14.2 Ma as inferred from our proxy records from the EAS, i.e., decreased mixing and shoaling of the thermocline, fits well into the emerging picture of an earlier intensification of the SAM since ~14.7 Ma (Zhuang et al., 2017; Bialik et al., 2020; Auer et al., 2023).

5.3. Factors driving summer SAM changes during the middle Miocene

The evolution and driving mechanisms of the summer SAM during the middle Miocene are strongly debated. Recent model simulations invoke a combination of orography (gradual uplift of the Himalayan-

Tibetan plateau; Eastern African and Anatolian-Iranian landforms), expanding ice sheets (glaciation in Antarctica), atmospheric CO_2 and orbital forcing for the strengthening of SAM rainfall after ~15 Ma (e.g., Farnsworth et al., 2019; Thomson et al., 2021; Zhang et al., 2014; Sarr et al., 2022; Tardif et al., 2023). In addition, Zhang et al. (2023) suggested that the stronger SAM during the global cooling at the time of MMCT is mainly attributed to the closure of the Tethyan Seaway, which can explain much of the sedimentary records for the SAM rainfall evolution (e.g., Yang et al., 2020; Ali et al., 2021). Here we suggest another factor, which may have contributed to drive changes in the summer SAM during the middle Miocene. At present, the summer SAM is driven by the cross-equatorial pressure gradient between the Indian Low over the Asian continent and the Mascarene High in the southern Indian Ocean (e.g., Webster and Fasullo, 2003). The Indian Low is driven by direct sensible heating of the Asian continent, particularly heating of the non-elevated parts of India, and by subsequent latent heat release due to moisture supply from the Indian Ocean (Webster and Fasullo, 2003). The Mascarene High is driven by the subsiding branch of the Southern Hemisphere Hadley cell because of the Equator-to-Antarctica temperature gradient. Modern observations show that colder-than-normal Antarctic temperatures lead to a stronger Mascarene High, which tends to strengthen the cross-equatorial Somali jet and thus the SAM (Xue et al., 2004). In addition, modern observational data also show that high (low) ice phase corresponds respectively to the strengthening (weakening) of the Mascarene High as well as an increase (decrease) in summer SAM rainfall (Azar et al., 2020). Azar et al. (2020) also found strong anticyclonic (cyclonic) anomalies in the Mascarene High region in 850 hPa winds, which led to corresponding strong (weak) south westerlies and thus respective positive (negative) summer SAM rainfall anomalies. The increase in rainfall in the SAM region at around ~14.5–14 Ma is in relatively good agreement with Southern Hemisphere surface ocean water cooling and Antarctic cryosphere expansion (Fig. 6). We therefore suggest that the increase in rainfall in the SAM region around ~14.5 to 14.0 Ma is most likely attributed to a stronger Mascarene High, which increased the cross-equatorial circulation and thus the summer SAM. A similar mechanism has been invoked to explain glacial-interglacial changes of the SAM during the Pleistocene (Rohling et al., 2009; An et al., 2011). This is also in good agreement with the proposed northward movement of the southern Westerly Winds and the Hadley cell in the Indian Ocean from the middle to the late Miocene (Groeneveld et al., 2017). In addition, an increase in SAM strength around ~14.5 to 14 Ma may also explain a stronger westerly jet over Central Asia during and after the MMCT (Frisch et al., 2019). To conclude, the intensification of the SAM during and after the MMCT fits well into the picture of a global reorganization of the atmospheric circulation following the expansion of the Antarctic ice sheets from ~14.7 to 13.8 Ma.

6. Conclusions

Drastic changes in SAM atmospheric circulation occurred during the MMCT (~14.7–13.0 Ma) period as inferred from proxy reconstructions from the WAS and model simulations. This study was aimed to investigate the impact of these monsoonal changes on the surface water hydrography in the EAS. To this end, the difference in Mg/Ca-based temperatures ($\Delta T°C$) of surface-dwelling with lower mixed layer/thermocline-dwelling and sub-thermocline-dwelling planktic foraminifera was calculated to estimate the upper ocean thermal gradient at Site NGHP-01-01 A in the EAS and thus changes in the upper surface water hydrography, i.e., depth of the mixed layer and thermocline. Our reconstructions reveal weaker mixing, a shallower thermocline, and therefore a well stratified upper water column in the EAS after ~14.2 Ma. We suggest that the weaker mixing and shallower thermocline in the EAS after ~14.2 Ma is most likely due to an intensification of the summer SAM. A strong salinity stratification and/or the formation of a barrier layer (BL) because of increased rainfall, higher river runoff from the Western Ghats and the intrusion of low salinity waters from the Bay of Bengal during the winter SAM may also have contributed to a weaker mixing and shallower thermocline in the EAS during the investigated time period. However, the latter scenario cannot yet be fully proven by substantial datasets because we lack winter EAM proxy records for the development and establishment of the modern winter SAM current surface circulation in the Indian Ocean during the middle Miocene. It is imperative that the latter scenario of this study is further validated by future studies of the winter SAM during the middle Miocene. Overall, our data for changes in the upper ocean hydrography in the EAC after ~14.2 Ma fits well with the emerging picture of monsoonal-driven upper ocean hydrographic changes in the equatorial and northern Indian Ocean due to an intensification of the summer SAM since ~14.7 Ma.

CRediT authorship contribution statement

Shixian Zou: Investigation, Writing – original draft, Writing – review & editing. **Guanyu Lin:** Investigation, Writing – original draft, Writing – review & editing. **Anran Chen:** Investigation, Writing – original draft, Writing – review & editing. **Yueli Huang:** Investigation, Writing – original draft, Writing – review & editing. **Jeroen Groeneveld:** Conceptualization, Writing – original draft, Writing – review & editing. **Stephan Steinke:** Conceptualization, Funding acquisition, Supervision, Writing – original draft, Writing – review & editing. **Liviu Giosan:** Conceptualization, Writing – original draft, Writing – review & editing.

Declaration of competing interest

The authors declare that they have no known competing financial interests or personal relationships that could have appeared to influence the work reported in this paper.

Data availability

Data of this manuscript are archived at PANGAEA-Data Publisher for Earth and Environmental Science. After acceptance we will add the link.

Acknowledgements

This study has been funded by the National Natural Science Foundation of China through a grant to S. Steinke (NSFC grant No. 41776055). We express our gratitude to H. Kuhnert (MARUM, University of Bremen) and his team for stable isotope analyses. L. Giosan acknowledges funding from USSP and WHOI and thanks colleagues and crew from the NGHP-01 expedition for help in acquiring core material. J. Groeneveld thanks the State Key Laboratory of Marine Environmental Science (Xiamen University) for a MEL Senior Visiting Fellowship (Project No. MELRS1915). We thank Y. Chen for her help with the planktic foraminiferal trace element analyses.

Appendix A. Supplementary data

Supplementary data to this article can be found online at https://doi.org/10.1016/j.palaeo.2024.112217.

References

Ali, S., Hathorne, E.C., Frank, M., 2021. Persistent provenance of south asian monsoon induced silicate weathering over the past 27 million years. Paleoceanogr. Paleoclimatol. 36 https://doi.org/10.1029/2020pa003909.

An, Z.S., Clemens, S.C., Shen, J., Qiang, X., Jin, Z., Sun, Y., Prell, W.L., Luo, J., Wang, S., Xu, H., Cai, Y., Zhou, W., Liu, X., Liu, W., Shi, Z., Yan, L., Xiao, X., Chang, H., Wu, F., Ai, L., Lu, F., 2011. Glacial-interglacial Indian summer monsoon dynamics. Science 333, 719–723. https://doi.org/10.1126/science.1203752.

Anand, P., Elderfield, H., Conte, M.H., 2003. Calibration of Mg/Ca thermometry in planktonic foraminifera from a sediment trap time series. Paleoceanography 18, 1050. https://doi.org/10.1029/2002PA000846.

Antonov, J.I., Seidov, D., Boyer, T.P., Locarnini, R.A., Mishonov, A.V., Garcia, H.E., Baranova, O.K., Zweng, M.M., Johnson, D.R., 2010. World Ocean Atlas 2009 volume 2: Salinity. In: Levitus, S. (Ed.), NOAA Atlas NESDIS 69, U.S. Gov. Printing Office, Washington, D.C., p. 184. http://www.nodc.noaa.gov/OC5/indprod.html

Antony, M.K., 1990. Northward undercurrent along west coast of India during upwelling-some inferences. Indian J. Mar. Sci. 19, 95–101. http://drs.nio.org/drs/handle/2264/2566.

Auer, G., Bialik, O.M., Antoulas, M.-E., Vogt-Vincent, N., Piller, W.E., 2023. Biotic response of plankton communities to Middle to late Miocene monsoon wind and nutrient flux changes in the Oman margin upwelling zone. Clim. Past 19, 2313–2340. https://doi.org/10.5194/cp-19-2313-2023.

Azar, S.S.A., Chenoli, S.N., Samah, A.A., Kim, S.-J., 2020. The linkages between Antarctic Sea ice extent and Indian summer monsoon rainfall. Polar Sci. 25 https://doi.org/10.1016/j.polar.2020.100537.

Barker, S., Greaves, M., Elderfield, H., 2003. A study of cleaning procedures used for foraminiferal Mg/ca paleothermometry. Geochem. Geophys. Geosyst. 4, 8407. https://doi.org/10.1029/2003GC000559.

Beasley, C., Kender, S., Giosan, L., Bolton, C.T., Anand, P., Leng, M.J., et al., 2021. Evidence of a South Asian proto-monsoon during the Oligocene-Miocene transition. Paleoceanogr. Paleoclimatol. 36, e2021PA004278 https://doi.org/10.1029/2021PA004278.

Behara, A., Vinayachandran, P.N., Shankar, D., 2019. Influence of rainfall over Eastern Arabian Sea on its salinity. J. Geophys. Res. Oceans 124, 5003–5020. https://doi.org/10.1029/2019JC014999.

Bemis, B.E., Spero, H.J., Bijma, J., Lea, D.W., 1998. Reevaluation of the oxygen isotopic composition of planktonic foraminifera: Experimental results and revised paleotemperature equations. Paleoceanography 13, 150–160. https://doi.org/10.1029/98PA00070.

Betzler, C., Eberli, G.P., Kroon, D., Wright, J.D., Swart, P.K., Nath, B.N., Alvarez-Zarikian, C.A., Alonso-García, M., Bialik, O.M., Blättler, C.L., Guo, J.A., Haffen, S., Horozal, S., Inoue, M., Jovane, L., Lanci, L., Laya, J.C., Hui Mee, A.L., Lüdmann, T., Nakakuni, M., Niino, K., Petruny, L.M., Pratiwi, S.D., Reijmer, J.J.G., Reolid, J., Slagle, A.L., Sloss, C.R., Su, X., Yao, Z., Young, J.R., 2016. The abrupt onset of the modern South Asian Monsoon winds. Sci. Rep. 6 https://doi.org/10.1038/srep29838.

Bialik, O.M., Frank, M., Betzler, C., Zammit, R., Waldmann, N.D., 2019. Two-step closure of the Miocene Indian Ocean Gateway to the Mediterranean. Sci. Rep. 9, 8842. https://doi.org/10.1038/s41598-019-45308-7.

Bialik, O.M., Auer, G., Ogawa, N.O., Kroon, D., Waldmann, N.D., Ohkouchi, N., 2020. Monsoons, upwelling, and the deoxygenation of the northwestern Indian Ocean in response to middle to late Miocene global climatic shifts. Paleoceanogr. Paleoclimatol. 35, e2019PA003762 https://doi.org/10.1029/2019PA003762.

Boyle, E.A., Keigwin, L.D., 1985. Comparison of Atlantic and Pacific paleochemical records for the last 215,000 years: changes in deep ocean circulation and chemical inventories. Earth Planet. Sci. Lett. 76, 135–150.

Broecker, W.S., Peng, T.H., 1982. Tracers in the Sea. Eldigo Press, Lamont-Doherty Geological Observatory, Columbia University, Palisades, New York, p. 690.

Burkill, P.H., Mantoura, R.F.C., Owens, N.J.P., 1993. Biogeochemical cycling in the northwestern Indian Ocean: a brief overview. Deep-Sea Res. II Top. Stud. Oceanogr. 40, 643–649. https://doi.org/10.1016/0967-0645(93)90049-S.

Collett, T., Riedel, M., Cochran, J., Boswell, R., Presley, J., Kumar, P., Sathe, A., Sethi, A., Lall, M., the NGHP Expedition Scientists, 2007. Indian National Gas Hydrate Program Expedition 01 report, U.S. Geological Survey Scientific Investigations Report, pp. 2012–5054, 1442 pp. https://doi.org/10.3133/sir20125054.

Durand, F., Shetye, S.R., Vialard, J., Shankar, D., Shenoi, S.S.C., Ethe, C., Madec, G., 2004. Impact of temperature inversions on SST evolution in the southeastern Arabian Sea during the pre-summer monsoon season. Geophys. Res. Lett. 31 https://doi.org/10.1029/2003GL18906.

Erez, J., Honjo, S., 1981. Comparison of isotopic composition of planktonic foraminifera in plankton tows, sediment traps and sediment. Palaeogeogr. Palaeoclimatol. Palaeoecol. 33, 129–156. https://doi.org/10.1016/0031-0182(81)90035-3.

Evans, D., Müller, W., 2012. Deep time foraminifera Mg/Ca paleothermometry: nonlinear correction for secular change in seawater Mg/Ca. Paleoceanography 27, PA4205. https://doi.org/10.1029/2012PA002315.

Evans, D., Brierley, C., Raymo, M.E., Erez, J., Müller, W., 2016. Planktic foraminifera shell chemistry response to seawater chemistry: Pliocene-Pleistocene seawater Mg/Ca, temperature and sea level change. Earth Planet. Sci. Lett. 438, 139–148. https://doi.org/10.1016/j.epsl.2016.01.013.

Fairbanks, R.G., Wiebe, P.H., Be, A.W.H., 1980. Vertical distribution and isotopic composition of living planktonic foraminifera in the western North Atlantic. Science 207, 61–63. https://doi.org/10.1126/science.207.4426.61.

Fairbanks, R.G., Sverdlove, M., Free, R., Wiebe, P.H., Be, A.W.H., 1982. Vertical distribution and isotopic fractionation of living planktonic foraminifera from the Panama Basin. Nature 298, 841–844. https://doi.org/10.1038/298841a0.

Farnsworth, A., Lunt, D.J., Robinson, S.A., Valdes, P.J., Roberts, W.H.G., Clift, P.D., Markwick, P., Su, T., Wrobel, N., Bragg, F., Kelland, S.-J., Pancost, R.P., 2019. Past East Asian monsoon evolution controlled by paleogeography, not CO_2. Sci. Adv. 5, eaax1697 https://doi.org/10.1126/sciadv.aax1697.

Findlater, J., 1969. A major low-level air current near the Indian Ocean during the northern summer. Q. J. R. Meteorol. Soc. 95, 362–380. https://doi.org/10.1002/qj.49709540409.

Frisch, K., Voigt, S., Verestek, V., Appel, E., Albert, R., Gerdes, A., Arndt, I., Raddatz, J., Voigt, T., Weber, Y., Batenburg, S.J., 2019. Long-period astronomical forcing of Westerlies' strength in Central Asia during Miocene climate cooling. Paleoceanogr. Paleoclimatol. 34 https://doi.org/10.1029/2019PA003642.

Gadgil, S., 2003. The Indian Monsoon and its variability. Annu. Rev. Earth Planet. Sci. 31, 429–467. https://doi.org/10.1146/annurev.earth.31.100901.141251.

Gaspari, J.T., Kennett, J.P., 1993. Vertical thermal structure evolution of Miocene surface waters; western Equatorial Pacific DSDP Site 289. Mar. Micropaleontol. 22, 235–254. https://doi.org/10.1016/0377-8398(93)90046-Z.

Groeneveld, J., Henderiks, J., Renema, W., McHugh, C.M., De Vleeschouwer, D., Christensen, B.A., Fulthorpe, C.S., Reuning, L., Gallagher, S.J., Bogus, K., Auer, G., Ishiwa, T., Expedition 356 Scientists, 2017. Australian shelf sediments reveal shifts in Miocene Southern Hemisphere westerlies. Sci. Adv. 3, e1602567 https://doi.org/10.1126/sciadv.1602567.

Gupta, A.K., Yuvaraja, A., Prakasam, M., Clemens, S.C., Velu, A., 2015. Evolution of the South Asian monsoon wind system since the late Middle Miocene. Palaeogeogr. Palaeoclimatol. Palaeoecol. 438, 160–167. https://doi.org/10.1016/j.palaeo.2015.08.006.

Hamon, N., Sepulchre, P., Lefebvre, V., Ramstein, G., 2013. The role of eastern Tethys seaway closure in the Middle Miocene Climatic transition (ca. 14 Ma). Clim. Past 9, 2687–2702. https://doi.org/10.5194/cp-9-2687-2013.

Hemleben, C., Spindler, M., Anderson, O.R., 1989. Modern Planktonic Foraminifera. Springer, New York, p. 363.

Holbourn, A.E., Kuhnt, W., Clemens, S.C., Kochhann, K.G., Jöhnck, J., Lübbers, J., Andersen, N., 2018. Late Miocene climate cooling and intensification of southeast Asian winter monsoon. Nat. Commun. 9 https://doi.org/10.1038/s41467-018-03950-1.

Jalihal, C., Bosmans, J.H.C., Srinivasan, J., Chakraborty, A., 2019. The Response of Tropical Precipitation to Earth's Precession: the Role of Energy Fluxes and Vertical Stability. Clim. Past 15, 449–462. https://doi.org/10.5194/cp-15-449-2019.

Karas, C., Nürnberg, D., Gupta, A.K., Tiedemann, R., Mohan, K., Bickert, T., 2009. Mid-Pliocene climate change amplified by a switch in Indonesian subsurface throughflow. Nat. Geosci. 2, 434–437. https://doi.org/10.1038/NGEO520.

Keerthi, M.G., Lengaigne, M., Vialard, J., de Boyer Montegut, C., Muraleedharan, P.M., 2013. Interannual variability of the Tropical Indian Ocean mixed layer depth. Clim. Dyn. 40, 743–759. https://doi.org/10.1007/s00382-012-1295-2.

Kiefer, T., McCave, I.N., Elderfield, H., 2006. Antarctic control on tropical Indian Ocean Sea surface temperature and hydrography. Geophys. Res. Lett. 33 https://doi.org/10.1029/2006GL027097.

Krishnan, R., Ramesh, K.V., Samala, B.K., Meyers, G., Slingo, J.M., Fennessy, M.J., 2006. Indian Ocean-monsoon coupled interactions and impending monsoon droughts. Geophys. Res. Lett. 33 https://doi.org/10.1029/2006GL025811.

Kroon, D., Steens, T., Troelstra, S.R., 1991. Onset of monsoonal related upwelling in the western Arabian Sea as revealed by planktonic foraminifers. In: Prell, W.L., Niitsuma, N., et al. (Eds.), Proceedings of the Ocean Drilling Program, Scientific Results 117. Ocean Drilling Program, College Station, Texas, pp. 257–263. https://doi.org/10.2973/odp.proc.sr.117.126.1991.

Lear, C.H., Coxall, H.K., Foster, G.L., Lunt, D.J., Mawbey, E.M., Rosenthal, Y., Sosdian, S.M., Thomas, E., Wilson, P.A., 2015. Neogene ice volume and ocean temperatures: Insights from infaunal foraminiferal Mg/Ca paleothermometry. Paleoceanography 30, 1437–1454. https://doi.org/10.1002/2015PA002833.

Li, G., Cheng, H., Pan, Y., Wang, G., Liu, H., Zhu, J., Zhang, B., Ren, H., Wang, X., 2023. A global gridded ocean salinity dataset with 0.5° horizontal resolution since 1960 for the upper 2000 m. Front. Mar. Sci. 10 https://doi.org/10.3389/fmars.2023.1108919.

Liu, Z., Yang, H., 2003. Extratropical control of tropical climate, the atmospheric bridge and oceanic tunnel. Geophys. Res. Lett. 30 https://doi.org/10.1029/2002GL016492.

Locarnini, R.A., Mishonov, A.V., Antonov, J.I., Boyer, T.P., Garcia, H.E., Baranova, O.K., Zweng, M.M., Johnson, D.R., 2010. World Ocean Atlas 2009. In: Levitus, S. (Ed.), Temperature, Vol. 1. NOAA Atlas NESDIS 68, U.S. Gov. Printing Office, Washington, D.C, p. 184. http://www.nodc.noaa.gov/OC5/indprod.html, 2010.

Madhupratap, M., Kumar, S.P., Bhattathiri, P.M.A., Kumar, M.D., Raghukumar, S., Nair, K.K.C., Ramaiah, N., 1996. Mechanism of the biological response to winter cooling in the northeastern Arabian Sea. Nature 384, 549–552. https://doi.org/10.1038/384549a0.

Mathew, B., Hareesh Kumar, P.H., Rao, R.R., 2003. Mixed layer variability at selected locations in the Arabian Sea during pre and summer monsoon seasons: Observations and simulations. Mausam 54, 917–928. https://doi.org/10.54302/mausam.v54i4.1592.

Milliman, J.D., Farnsworth, K.L., 2011. River Discharge to the Coastal Ocean: A Global Synthesis. Cambridge University Press, Cambridge, p. 392. https://doi.org/10.1017/CBO9780511781247.

Mohtadi, M., Oppo, D.W., Lückge, A., DePol-Holz, R., Steinke, S., Groeneveld, J., Hemme, N., Hebbeln, D., 2011. Reconstructing the thermal structure of the upper ocean: Insights from planktic foraminifera shell chemistry and alkenones in modern sediments of the tropical eastern Indian Ocean. Paleoceanography 26. https://doi.org/10.1029/2011PA002132.

Mohtadi, M., Prange, M., Oppo, D.W., De Pol-Holz, R., Merkel, U., Zhang, X., Steinke, S., Lückge, A., 2014. North Atlantic forcing of tropical Indian Ocean climate. Nature 509, 76–80. https://doi.org/10.1038/nature13196.

Muggeo, V.M.R., 2008. Segmented: An R Package to Fit Regression Models with Broken-Line Relationships. R News 8, pp. 20–25. https://cran.r-project.org/doc/Rnews/.

Muraleedharan, P.M., Kumar, M.R., Rao, L.G., 1995. A note on poleward undercurrent along the southwest coast of India. Cont. Shelf Res. 15, 165–184. https://doi.org/10.1016/0278-4343(94)E0021-D.

Naqvi, S.W.A., Naik, H., Pratihary, A., D'Souza, W., Narvekar, P.V., Jayakumar, D.A., Devol, A.H., Yoshinari, T., Saino, T., 2006. Coastal versus open-ocean denitrification in the Arabian Sea. Biogeosciences 3, 621–633. https://doi.org/10.5194/bg-3-621-2006.

Parthasarathy, B., Dhar, O.N., 1974. Secular variations of regional rainfall over India. Q. J. R. Meteorol. Soc. 100, 245–257. https://doi.org/10.1002/qj.49710042411.
Pearson, P.N., Shackleton, N.J., 1995. Neogene Multispecies planktonic foraminifer stable isotope record, Site 871, Limalok Guyot. In: Proceedings of the Ocean Drilling Program, Scientific Results, 144, pp. 401–407.
Pearson, P.N., Wade, B.S., 2009. Taxonomy and stable isotope paleoecology of well-preserved planktonic foraminifera from the uppermost Oligocene of Trinidad. J. Foraminifer. Res. 39, 191–217. https://doi.org/10.2113/gsjfr.39.3.191.
Pearson, P.N., Shackleton, N.J., Weedon, G.P., Hall, M.A., 1997. Multi-species planktonic foraminifer stable isotope stratigraphy through Oligocene/Miocene boundary climatic cycles, ODP Site 926. Proc. Ocean Drill. Prog. Sci. Res. 154, 441–450. https://doi.org/10.2973/odp.proc. sr.154.118.1997.
Pena, L.D., Goldstein, S.L., Hemming, S.R., Jones, K.M., Calvo, E., Pelejero, C., Cacho, I., 2013. Rapid changes in meridional advection of Southern Ocean intermediate waters to the tropical Pacific during the last 30 kyr. Earth Planet. Sci. Lett. 368, 20–32. https://doi.org/10.1016/j.epsl.2013.02.028.
Podder, R.S., Gupta, A.K., Clemens, S., 2021. Surface paleoceanography of the eastern equatorial Indian Ocean since the latest Miocene: Foraminiferal census and isotope records from ODP Site 758A. Palaeogeogr. Palaeoclimatol. Palaeoecol. 579, 110617 https://doi.org/10.1016/j.palaeo.2021.110617.
Podder, R.S., Gupta, A.K., Clemens, S., Sanyal, P., Panigrahi, M.K., 2024. Changes in the Indian Ocean surface hydrography driven by the seaway closure and monsoonal circulation since the late Oligocene. Glob. Planet. Chang. 232, 104335 https://doi.org/10.1016/j.gloplacha.2023.104335.
Prasad, T., Ikeda, M., Kumar, S.P., 2001. Seasonal spreading of the Persian Gulf Water mass in the Arabian Sea. J. Geophys. Res. Oceans 106, 17059–17071. https://doi.org/10.1029/2000JC000480.
Prasanna Kumar, S., Narvekar, J., Kumar, A., Shaji, C., Anand, P., Sabu, P., Rijomon, G., Josia, J., Jayaraj, K.A., Radhika, A., Nair, K.K.C., 2004. Intrusion of the Bay of Bengal water into the Arabian Sea during winter monsoon and associated chemical and biological response. Geophys. Res. Lett. 31 https://doi.org/10.1029/2004GL020247.
Qu, T., Meyers, G., 2005. Seasonal variation of barrier layer in the southeastern tropical Indian Ocean. J. Geophys. Res. Oceans 110. https://doi.org/10.1029/2004JC002816.
Qu, T., Du, Y., Gan, J., Wang, D., 2007. Mean seasonal cycle of isothermal depth in the South China Sea. J. Geophys. Res. Oceans 112. https://doi.org/10.1029/2006JC003583.
Rao, R., Molinari, R., Festa, J., 1989. Evolution of the climatological nearsurface thermal structure of the tropical Indian Ocean: 1. Description of mean monthly mixed layer depth, and sea surface temperature, surface current, and surface meteorological fields. J. Geophys. Res. 94 https://doi.org/10.1029/JC094iC08p10801, 10,801-10,815.
Rohling, E.J., Liu, Q.S., Roberts, A.P., Stanford, J.D., Rasmussen, S.O., Langen, P.L., Siddall, M., 2009. Controls on the East Asian monsoon during the last glacial cycle, based on comparison between Hulu Cave and polar ice-core records. Quat. Sci. Rev. 28, 3291–3302. https://doi.org/10.1016/j.quascirev.2009.09.007.
Romahn, S., Mackensen, A., Groeneveld, J., Pätzold, J., 2014. Deglacial intermediate water reorganization: New evidence from the Indian Ocean. Clim. Past 10, 293–303. https://doi.org/10.5194/cp-10-293-2014.
Sarr, A.-C., Donnadieu, Y., Bolton, C.T., Ladant, J.-B., Licht, A., Fluteau, F., Laugié, M., Tardif, D., Dupont-Nivet, G., 2022. Neogene south Asian monsoon rainfall and wind histories diverged due to topographic effects. Nat. Geosci. 15, 314–319. https://doi.org/10.1038/s41561-022-00919-0.
Satpathy, R.K., Steinke, S., Singh, A.D., 2019. Monsoon-induced changes in surface hydrography of the eastern Arabian Sea during the early Pleistocene. Geol. Mag. https://doi.org/10.1017/S0016756819000098.
Schiebel, R., Zeltner, A., Treppke, U.F., Waniek, J.J., Bollmann, J., Rixen, T., Hemleben, C., 2004. Distribution of diatoms, coccolithophores and planktic foraminifers along a trophic gradient during SW monsoon in the Arabian Sea. Mar. Micropaleontol. 51, 345–371. https://doi.org/10.1016/j.marmicro.2004.02.001, 10.1038/s41561-022-00919-0.
Schott, F.A., McCreary Jr., J.P., 2001. The monsoon circulation of the Indian Ocean. Prog. Oceanogr. 5, 1–123. https://doi.org/10.1016/S0079-6611(01)00083-0.
Scotese, C.R., 2002. PALEOMAP website. http://www.scotese.com.
Shankar, D., Remya, R., Vinayachandran, P.N., Chatterjee, A., Behera, A., 2016. Inhibition of mixed-layer deepening during winter in the northeastern Arabian Sea by the West India Coastal Current. Clim. Dyn. 47, 1049–1072. https://doi.org/10.1007/s00382-015-2888-3.
Shenoi, S.S.C., Shankar, D., Shetye, S.R., 2004. Remote forcing annihilates barrier layer in southeastern Arabian Sea. Geophys. Res. Lett. 31 https://doi.org/10.1029/2003GL019270.
Sherin, C.K., Gupta, G.V.M., Sudheesh, V., Ramu, Ch.V., Reddy, B., Harikrishnachari, N. V., Kumar Vijayan, A., 2023. Nutriclines and nutrient stoichiometry in the eastern Arabian Sea: Intra-annual variations and controlling mechanisms. Prog. Oceanogr. 215, 103048 https://doi.org/10.1016/j.pocean.2023.103048.
Shetye, S.R., Gouveia, A.D., Shenoi, S.S.C., Sundar, D., Michael, G.S., Almeida, A.M., Santanam, K., 1990. Hydrography and circulation off the west coast of India during the southwest monsoon 1987. J. Mar. Res. 48, 359–378. https://doi.org/10.1357/002224090784988809.
Shetye, S., Gouveia, A., Shenoi, S., Michael, G., Sundar, D., Almeida, A., Santanam, K., 1991. The coastal current off western India during the northeast monsoon. Deep-Sea Res. 38, 1517–1529. https://doi.org/10.1016/0198-0149(91)90087-V.
Shevenell, A.E., Kennett, J.P., Lea, D.W., 2004. Middle Miocene southern Ocean cooling and Antarctic cryosphere expansion. Science 305, 1766–1770. https://doi.org/10.1126/science.1100061.
Shevenell, A.E., Kennett, J.P., Lea, D.W., 2008. Middle Miocene ice sheet dynamics, deep-sea temperatures, and carbon cycling: a Southern Ocean perspective. Geochem. Geophys. Geosyst. 9 https://doi.org/10.1029/2007GC001736.
Sprintall, J., Tomczak, M., 1992. Evidence of the barrier layer in the surface layer of the tropics. J. Geophys. Res. Oceans 97, 7305–7316. https://doi.org/10.1029/92JC00407.
Stanley, S.M., Hardie, L.A., 1998. Secular oscillations in the carbonate mineralogy of reef-building and sediment-producing organisms driven by tectonically forced shifts in seawater chemistry. Palaeogeogr. Palaeoclimatol. Palaeoecol. 144, 3–19. https://doi.org/10.1016/S0031-0182(98)00109-6.
Steinke, S., Mohtadi, M., Groeneveld, J., Lin, L.C., Löwemark, L., Chen, M.T., Rendle-Bühring, R., 2010. Reconstructing the southern South China Sea upper water column structure since the last Glacial Maximum: Implications for the East Asian winter monsoon development. Paleoceanography 25. https://doi.org/10.1029/2009PA001850.
Steinke, S., Glatz, C., Mohtadi, M., Groeneveld, J., Li, Q., Jian, Z., 2011. Past dynamics of the East Asian monsoon: no inverse behaviour between the summer and winter monsoon during the Holocene. Glob. Planet. Chang. 78, 170–177. https://doi.org/10.1016/j.gloplacha.2011.06.006.
Swapna, P., Krishnan, R., Wallace, J.M., 2014. Indian Ocean and monsoon coupled interactions in a warming environment. Clim. Dyn. 42, 2439–2454. https://doi.org/10.1007/s00382-013-1787-8.
Tardif, D., Sarr, A.-C., Fluteau, F., Licht, A., Kaya, M., Ladant, J.-B., Meijer, N., Donnadieu, Y., Dupont-Nivet, G., Bolton, C.T., Le Hir, G., Pillot, Q., Poblete, F., Sepulchre, P., Toumoulin, A., Banfield, W., 2023. The role of paleogeography in Asian monsoon evolution: a review and new insights from climate modelling. Earth Sci. Rev. 243, 104464. https://doi.org/10.1016/j.earscirev.2023.104464.
Thomson, J.R., Holden, P.B., Anand, P., Edwards, N.R., Porchier, C.A., Harris, N.B.W., 2021. Tectonic and climatic drivers of Asian monsoon evolution. Nat. Commun. 12 https://doi.org/10.1038/s41467-021-24244-z.
Tomas, R.A., Webster, P.J., 1997. The role of inertial instability in determining the location and strength of near-equatorial convection. Q. J. R. Meteorol. Soc. 123, 1445–1482. https://doi.org/10.1002/qj.49712354202.
Vijith, V., Vinayachandran, P., Thushara, V., Amol, P., Shankar, D., Anil, A., 2016. Consequences of inhibition of mixed-layer deepening by the West India Coastal Current for winter phytoplankton bloom in the northeastern Arabian Sea. J. Geophys. Res. Oceans 121, 6583–6603. https://doi.org/10.1002/2016JC012004.
Viswambharan, N., Mohanakumar, K., 2014. Modulation of Indian summer monsoon through northern and southern hemispheric extra-tropical oscillations. Clim. Dyn. 43, 925–938. https://doi.org/10.1007/s00382-014-2049-0.
Webster, P.J., Fasullo, J., 2003. Monsoon-dynamical theory. Encyclop. Atmos. Sci. 1370-1386 https://doi.org/10.1016/B0-12-227090-8/00236-0.
Webster, P.J., Magana, V.O., Palmer, T.N., Shukla, J., Tomas, R.A., Yanai, M.U., Yasunari, T., 1998. Monsoons: Processes, predictability, and the prospects for prediction. J. Geophys. Res. Oceans 103, 14451–14510. https://doi.org/10.1029/97JC02719.
Wilkinson, B., Algeo, T., 1989. Sedimentary carbonate record of calcium-magnesium cycling. Am. J. Sci. 289, 1158–1194. https://doi.org/10.2475/ajs.289.10.1158.
Woodruff, F., Savin, S.M., 1989. Miocene Deepwater oceanography. Paleoceanography 4, 87–140. https://doi.org/10.1029/PA004i001p00087.
Wright, J.D., Miller, K.G., Fairbanks, R.G., 1992. Early and middle Miocene stable isotopes: implications for Deepwater circulation and climate. Paleoceanography 7, 357–389. https://doi.org/10.1029/92PA00760.
Wyrtki, K., 1961. The thermohaline circulation in relation to the general circulation in the oceans. Deep-Sea Res. 8, 39–64. https://doi.org/10.1016/0146-6313(61)90014-4.
Xue, F., Wang, H., He, J., 2004. Interannual variability of mascarene high and Australian high and their influences on East Asian Summer Monsoon. J. Meteor. Soc. Japan 82, 1173–1186. https://doi.org/10.2151/jmsj.2004.1173.
Yang, X., Groeneveld, J., Jian, Z., Steinke, S., Giosan, L., 2020. Middle Miocene intensification of South Asian monsoonal rainfall. Paleoceanogr. Paleoclimatol. 35, e2020PA003853 https://doi.org/10.1029/2020PA003853.
You, Y., 1998. Intermediate water circulation and ventilation of the Indian Ocean derived from water-mass contributions. J. Mar. Res. 56, 1029–1067. https://doi.org/10.1357/002224098765173455.
Zhang, Z., Ramstein, G., Schuster, M., Li, C., Contoux, C., Yan, Q., 2014. Aridification of the Sahara desert caused by Tethys Sea shrinkage during the late Miocene. Nature 513, 401–404. https://doi.org/10.1038/nature13705.
Zhang, Jian, Yongyun, Hu, Zhu, Chenguang, Flögel, Sascha, Fang, Xiaomin, Sun, Jimin, 2023. Modeling the effects of global cooling and the Tethyan Seaway closure on North African and South Asian climates during the Middle Miocene Climate Transition. Palaeogeogr. Palaeoclimatol. Palaeoecol. 619, 111541 https://doi.org/10.1016/j.palaeo.2023.111541.
Zhuang, G., Pagani, M., Zhang, Y.G., 2017. Monsoonal upwelling in the western Arabian Sea since the middle Miocene. Geology 45. https://doi.org/10.1130/G39013.1, 655-658.
Zou, S., Groeneveld, J., Giosan, L., Steinke, S., 2022. Determining the habitat depth of the planktic foraminifera *Dentoglobigerina altispira* in the eastern Arabian Sea during the middle Miocene. Mar. Micropaleontol. 170, 102075 https://doi.org/10.1016/j.marmicro.2021.102075.